Analysis and Optimization Study of Shrouded Horizontal Axis Wind Turbines

Tariq Abdulsalam Khamlaj

Supervision:
Dr. Markus Peer Rumpfkeil

Department of Mechanical and Aerospace Engineering

August 24, 2018

Outline

Effect of Shroud

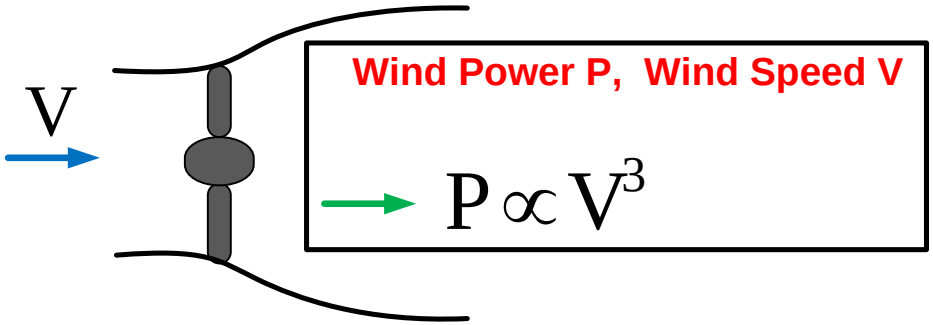

$$P = \frac{1}{2}\rho C_P A V^3$$

- Basic idea is to increase power output without necessarily increasing the size of the rotor.
- The concept of accelerating the wind is named the "Wind lens".

Wind Lens

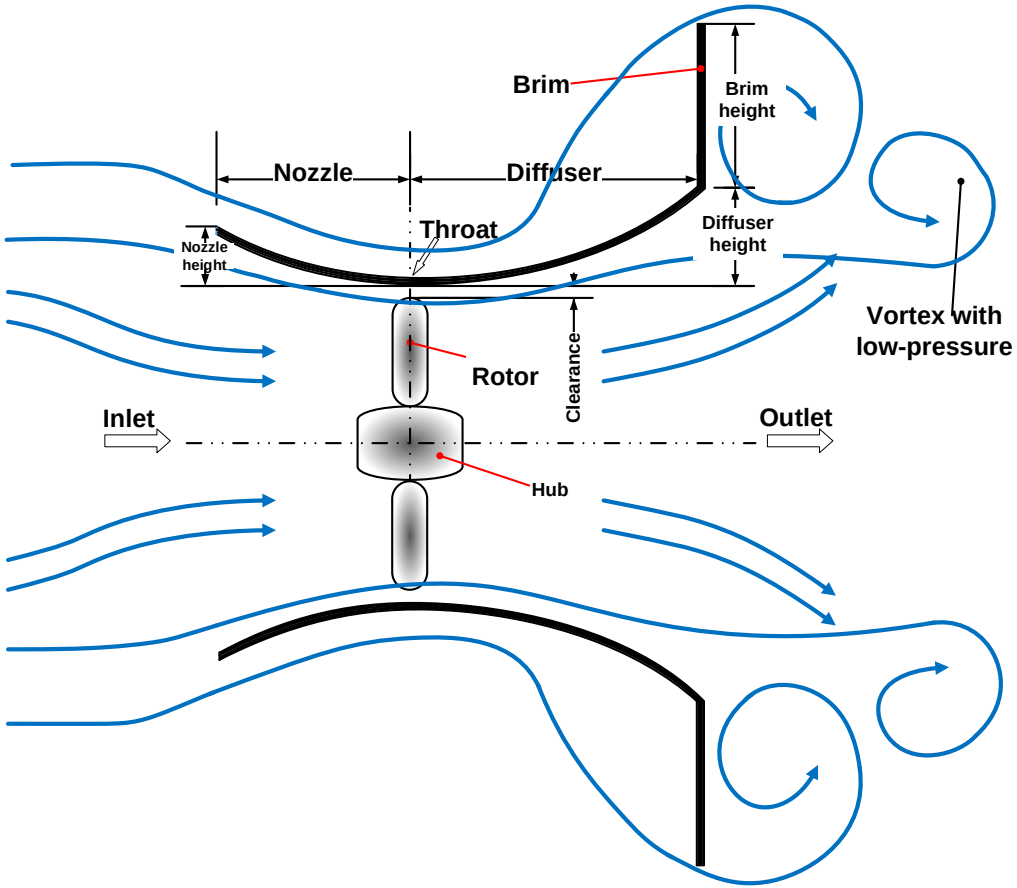

Figure 1 : Flow around and through wind turbine with brimmed diffuser (Wind-lens).

History

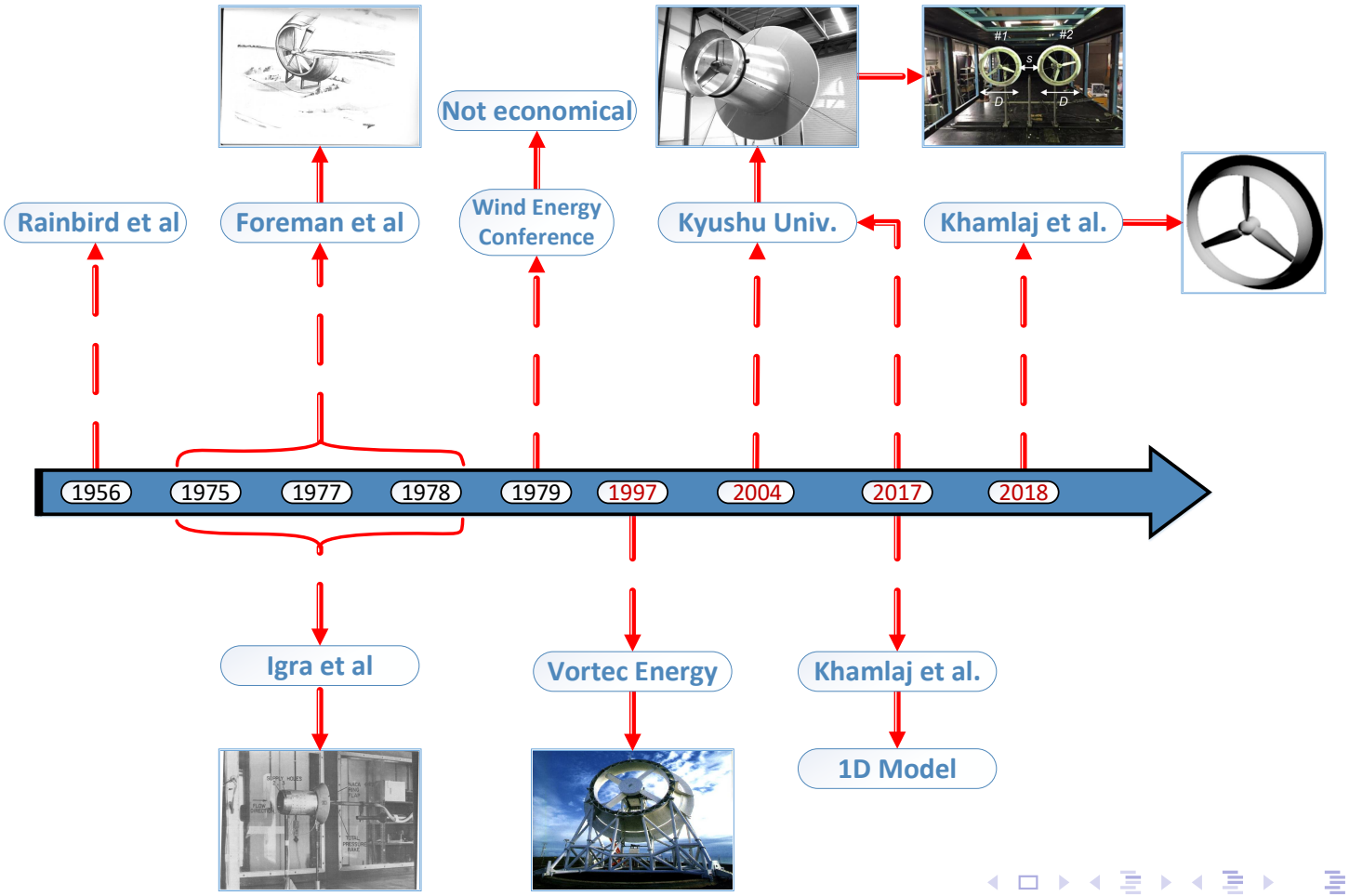
Rainbird et al
Foreman et al
Not economical
Wind Energy Conference
Kyushu Univ.
Khamlaj et al.
1956
1975
1977
1978
1979
1997
2004
2017
2018
Igra et al
Vortec Energy
Khamlaj et al.
1D Model

Objective

- Shrouded wind turbines with a brimmed diffuser have demonstrated power augmentation by a factor of about 4 to 5 compared with a bare wind turbine, for a given turbine diameter and wind speed [1, 2].
- The objective of this research is
  - to develop a fast and accurate simulation tool for the performance prediction and optimization of wind-lens turbines.
  - to improve the wind-lens efficiency by designing the duct and brim shape through an optimization process that maximizes the power while minimizing thrust and drag forces.

Semi-empirical 1D Model

Governing Equations;

- Conservation of Mass

$$\underbrace{\frac{\partial}{\partial t}\int_{CV}\rho d\forall}_{=0(5)}+\int_{CS}\rho\vec{V}\cdot d\vec{A}=0 \tag{1}$$

- Conservation of Momentum

$$\underbrace{\frac{\partial}{\partial t}\int_{CV}\vec{V}\rho d\forall}_{=0(5)}+\int_{CS}\vec{V}\rho\vec{V}\cdot d\vec{A}=\vec{F}_s+\underbrace{\vec{F}_B}_{=0(8)} \tag{2}$$

- 1st Law of Thermodynamics

$$\underbrace{\dot{Q}}_{=0(9)}-\underbrace{\dot{W}_s-\dot{W}_{shear}-\dot{W}_{other}}_{=0(9)}=\underbrace{\frac{\partial}{\partial t}\int_{CV}e\rho d\forall}_{=0(5)}+\int_{CS}\left(u+pv+\frac{V^2}{2}+gz\right)\rho\vec{V}\cdot d\vec{A} \tag{3}$$

Semi-empirical 1D Model

Figure 2 : Stream tube passing through a bare wind turbine.

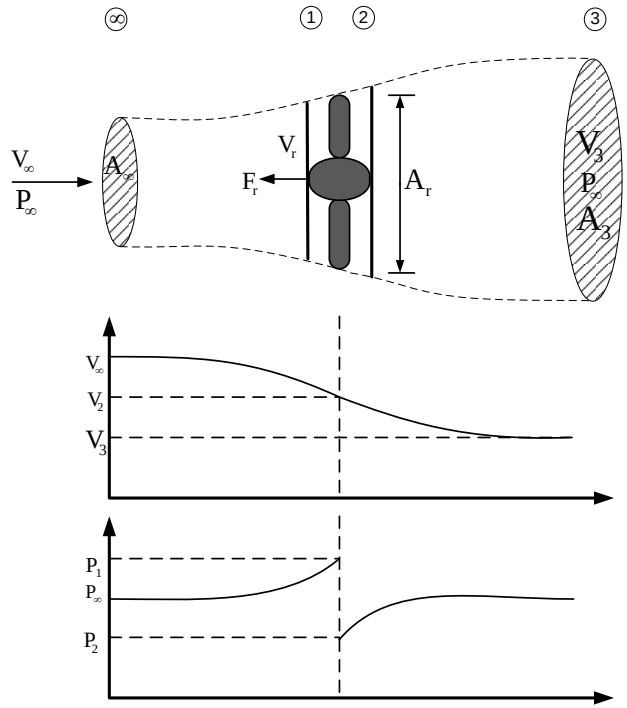

Assumptions for Derivation

- The turbine is represented as an actuator disc.
- The disc is considered ideal (frictionless).
- There is no rotational velocity component in the wake.
- The entire process is assumed to occur at a small Mach number, and the air density is thus constant (Incompressible flow).
- The flow is assumed to be steady.
- There are no external forces acting on the fluid up or down stream of the turbine.
- Body forces are negligible.
- $\dot{Q}$, $\dot{W_s}$, $\dot{W_{shear}}$, $\dot{W_{other}} = 0$.

Semi-empirical 1D Model

Table 1 : Summary of results for bare wind turbine and NDAWT.

Parameter	**Bare Wind Turbine**	**NDAWT**
Upstream wind speed	V_∞	V_∞
Wind speed at rotor plane	$V_\infty \cdot \frac{4}{\psi+4}$	$V_\infty \cdot \sqrt{\frac{1-C_{p_b}}{\psi+\eta_N+\lambda_N^2(1-\eta_N)-\eta_D\left(1-\lambda_D^2\right)}}$
Far wake wind speed	$V_\infty \cdot \frac{4-\psi}{\psi+4}$	$V_\infty \cdot \sqrt{C_{p_b}+\lambda_D^2\frac{V_1^2}{V_\infty^2}}$
Power coefficient C_P	$\frac{64\psi}{(\psi+4)^3}$	$\psi\left[\frac{1-C_{p_b}}{\psi+\eta_N+\lambda_N^2(1-\eta_N)-\eta_D\left(1-\lambda_D^2\right)}\right]^{\frac{3}{2}}$
Thrust coefficient C_t	$\frac{16\psi}{(\psi+4)^2}$	$\psi\left[\frac{1-C_{p_b}}{\psi+\eta_N+\lambda_N^2(1-\eta_N)-\eta_D\left(1-\lambda_D^2\right)}\right]$

Semi-empirical 1D Model

Table 2 : Parameters of a shrouded wind turbine used in [3].

Parameter	Value
Diffuser Area ratio λ_D	0.54
Density ρ	1.225 kg/m^3
The back pressure of the diffuser C_{p_b}	-0.38
The diffuser efficiency η_D	83%

Table 3 : Parameters of a shrouded wind turbine with a brim [2].

Parameter	Value
Turbine diameter D	0.7 m
Diffuser diameter D_e	1.072 m
Nozzle diameter D_N	0.78 m
Diffuser length L_t	1.029 m
The brim height h	0.35 m
Density ρ	1.225 kg/m^3
The back pressure of the diffuser C_{p_b}	-0.6
The nozzle efficiency η_N	85%
The diffuser efficiency η_D	85%

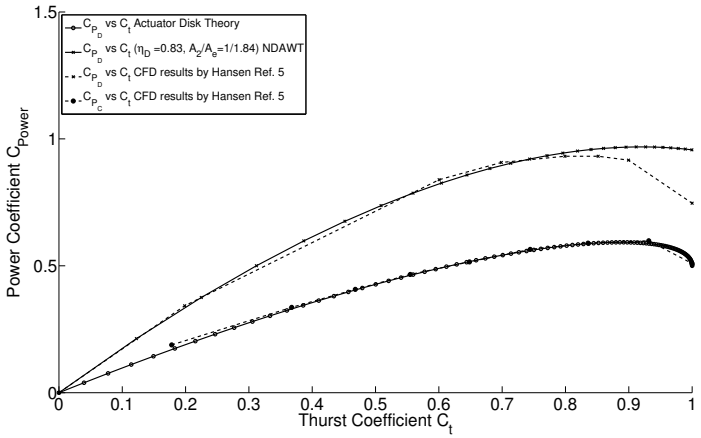

Figure 3 : Verification of the 1-D model.

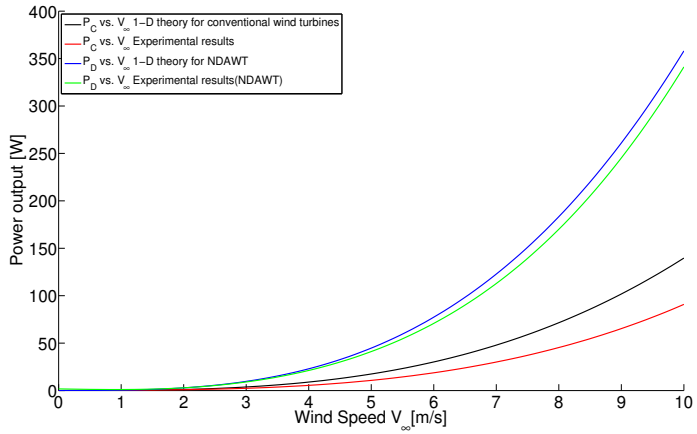

Figure 4 : Validation of the 1-D model.

CFD solver

- The computational analysis is performed with the Open source Field Operation And Manipulation (OpenFOAM) CFD code.
- The governing equations of the flow field solved by the simpleFoam solver are the steady state, incompressible form of the continuity and conservation of momentum equations.
- For the simulation of the effects of turbulence on the main flow, the *Spalart – Allmaras*, the $k-\epsilon$, and the $k-\omega$ Shear Stress Transport (SST) model are utilized.
- The computational meshes are generated using the open source tool Gmsh.

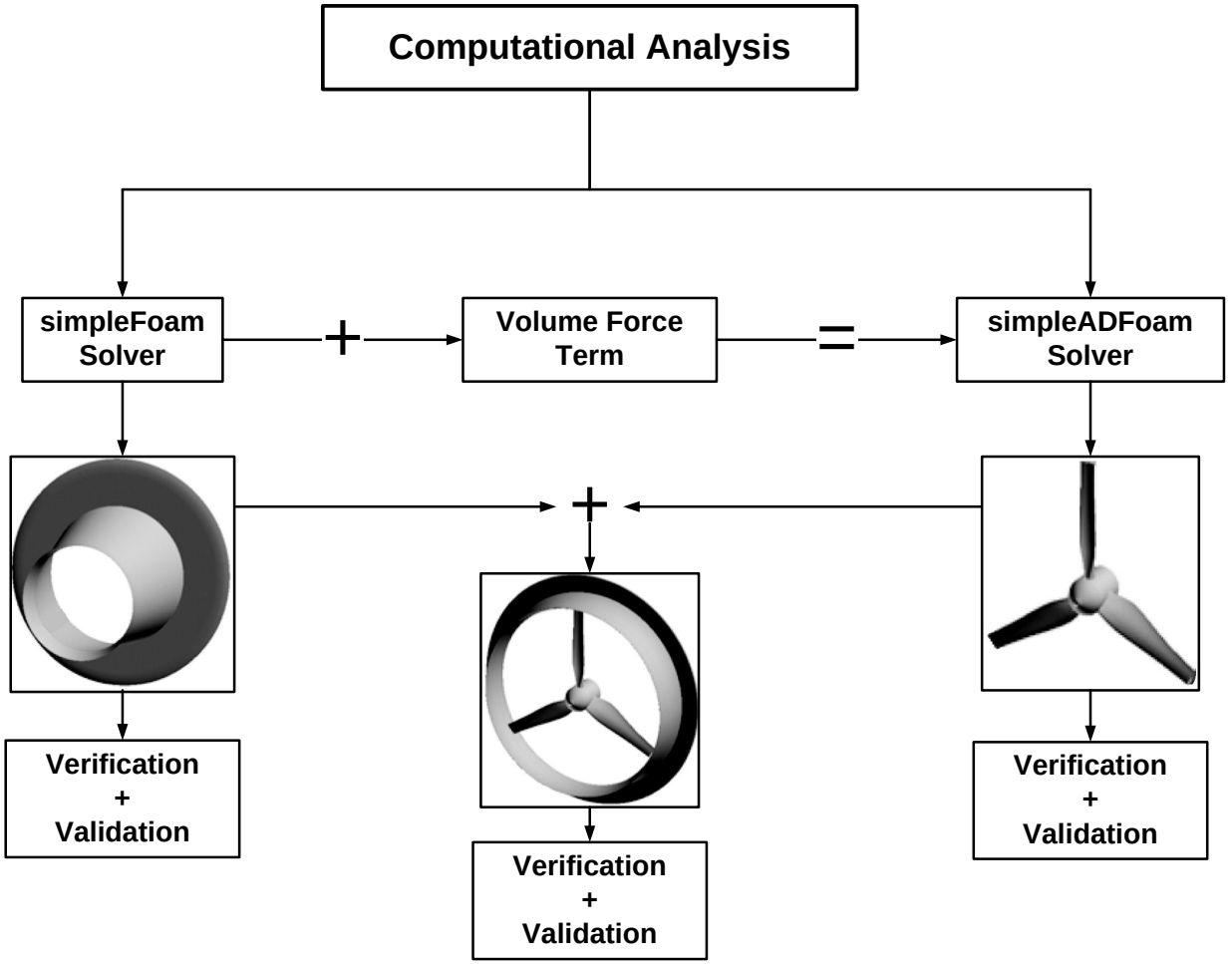
Computational Analysis
simpleFoam Solver
+
Volume Force Term
=
simpleADFoam Solver
+
Verification + Validation
Verification + Validation
Verification + Validation

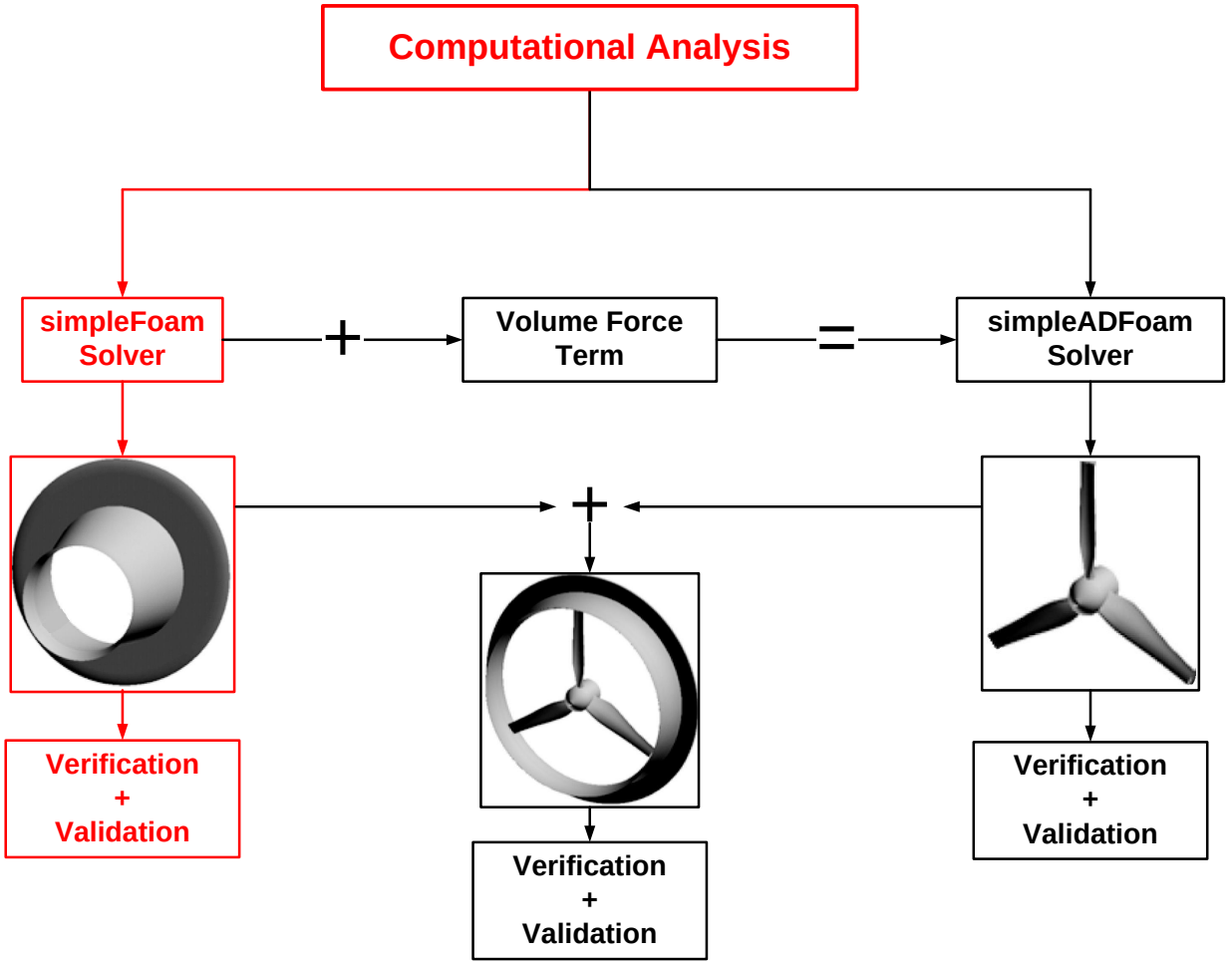
Computational Analysis
simpleFoam Solver
+
Volume Force Term
=
simpleADFoam Solver
Verification + Validation
Verification + Validation
Verification + Validation

Case Setup and Boundary Conditions

Table 4 : Detailed information for shrouded diffuser.

Experimental model	Long type [4]
Diameter of the throat D	600mm
Diameter of the hub D_h	0.22D
Height of the flange h	0.5D
Diffuser length L_D	1.25D
Inlet length L_N	0.25D
Tip clearance	10 mm
Semi-open angle θ	12^o
Inlet velocity V_∞	6 m/s

Table 5 : Fluid Properties.

Property	Value
Kinematic Viscosity ν	$1.5 \times 10^{-5} m^2/s^2$
Air Density ρ	$1.225 kg/m^3$
Reynolds No. Re	$2.2 \times 10^5 - 5.5 \times 10^5$

Table 6 : Pertinent discretization information.

Aspect	Description
Coordinates system	3-D
Computational grid	H-O type
Scheme	Finite volume method
Coupling algorithm	SIMPLE method
Laplacian schemes	Gauss limitedLinear
Gradient schemes	cellLimited $<$ *gradScheme* $>$
Divergence schemes	upwind

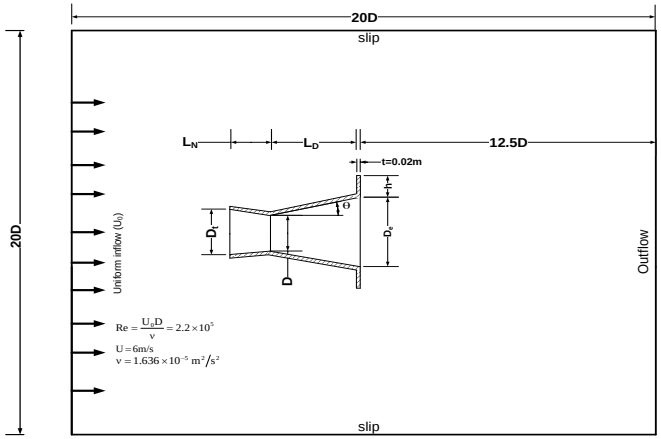

Figure 5 : Computational domain and BCs.

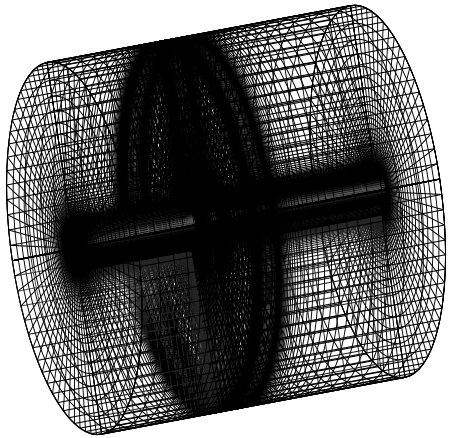

Figure 6 : Example for the 3D grid.

Grid Independence Study I

- Computational field: Cylindrical shape (length = 20D, Diameter=20D)
- The fluid is set to be air at a temperature of $25^{\circ}C$.
- The reference pressure is 1atm.
- Turbulent inflow: 6m/s, $I_0 = 3.1\%$, $k_0 = 0.05m^2/s^2$ and $\epsilon_0 = 0.026m^2$
- Outlet (pressure outlet): 0Pa
- Domain walls: free slip wall
- Diffuser walls: no slip walls with $k_{wall} = \epsilon_{wall} = 0$.

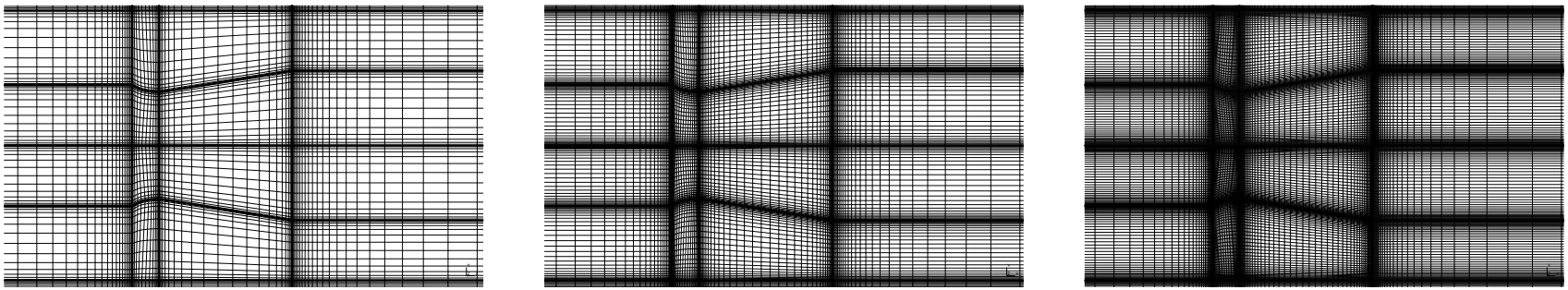

(a) No. of nodes 75672. (b) No. of nodes 116208. (c) No. of nodes 180384.

Figure 7 : Grids used with $k - \epsilon$ turbulence model for the grid independence study.

Grid Independence Study II

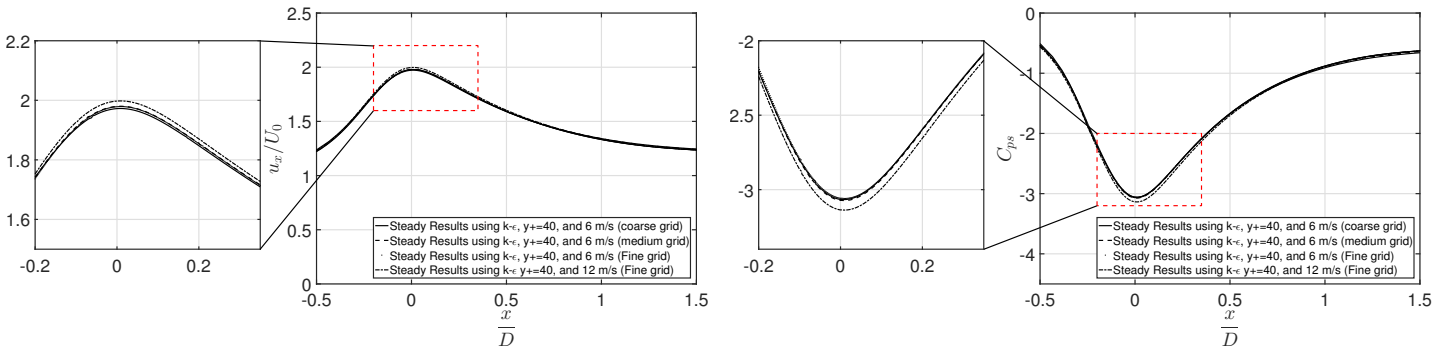

(a) Velocity distribution. (b) Pressure distribution.

Figure 8 : Velocity and pressure distribution for the three grids with $k-\epsilon$ turbulence model.

Figure 9 : Velocity, streamlines, and pressure distribution of the flow over an empty flanged diffuser.

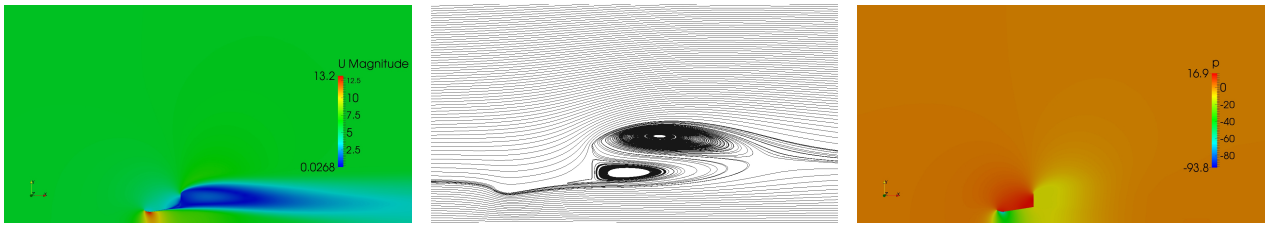

(a) V dist. using $k-\omega$. (b) Streamlines using $k-\omega$. (c) P dist. using $k-\omega$.

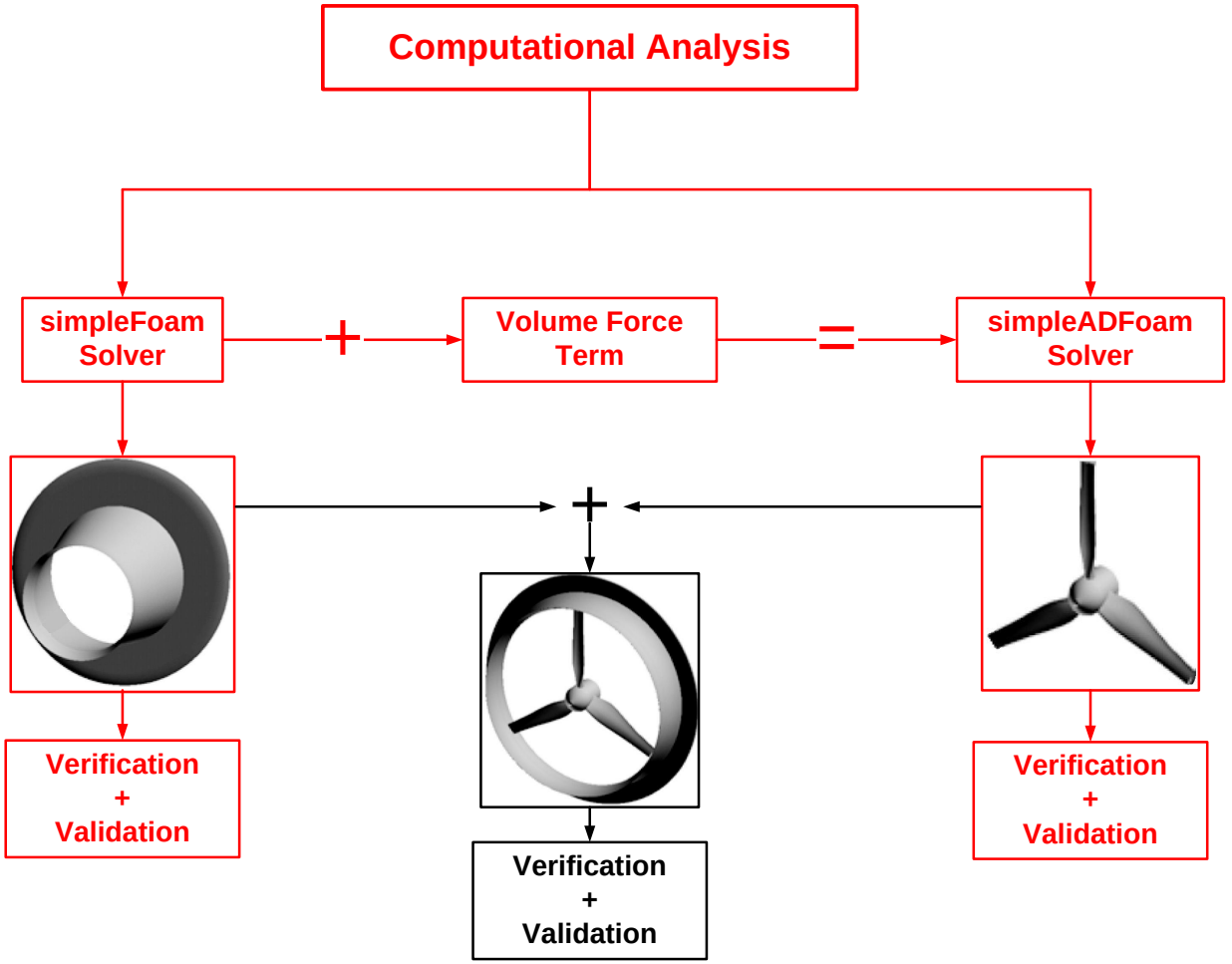
Computational Analysis
simpleFoam Solver
+
Volume Force Term
=
simpleADFoam Solver
Verification + Validation
Verification + Validation
Verification + Validation

Analysis of Wind Turbine

- Wind turbine aerodynamic simulations are important for developing future wind turbines.
- Three main methods of analysis are available:
  - Actuator Disk (AD) coupled with Blade Element Method (BEM).
  - Actuator Line (AL).
  - Fully resolved blade profile model (FR).

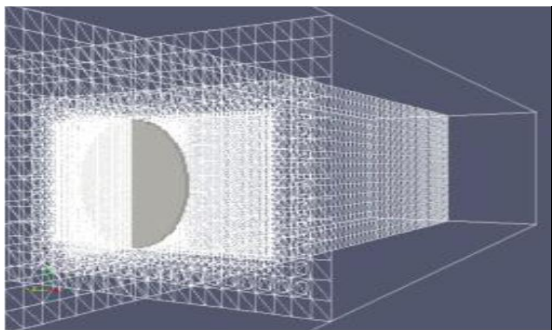

(d) AD.

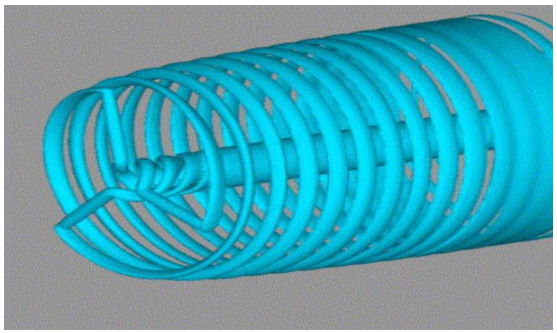

(e) AL [5].

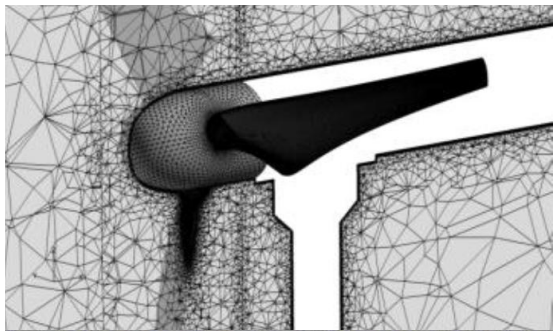

(f) FR [5].

Analysis of Wind Turbine

	Advantages	Disadvantages
AD+BEM	• Simple model. • Very low computational cost.	• Cannot reproduce detailed wake structure. • Input parameters are difficult to handle. • Need to rely on tabulated airfoil data.
AL	• Can potentially reproduce detailed wake structure. • Low computational cost.	• Input parameters are difficult to handle. • Need to rely on tabulated airfoil data.
FR	• Best Model in wake reproduction. • Does not rely on tabulated airfoil data.	• Very high computational cost and large meshing effort.

Blade element theory relies on two key assumptions:

- There are no aerodynamic interactions between different blade elements.
- The forces on the blade elements are solely determined by the lift and drag coefficients.

Governing Equations for BEM Used with AD Model

Figure 10 : Blade geometry for analysis of a horizontal axis wind turbine.

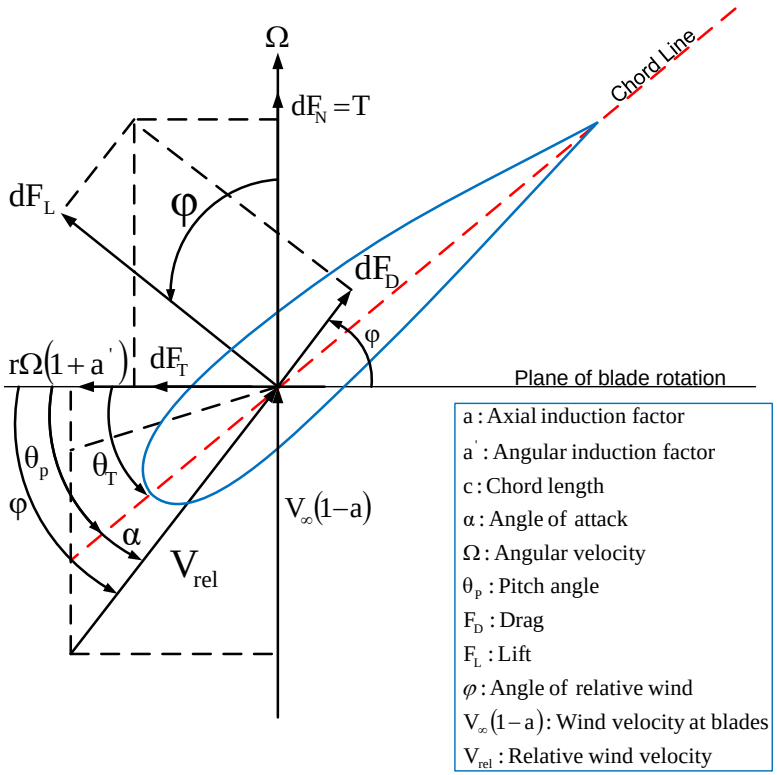

(a) F_L and F_D acting on a blade [6].

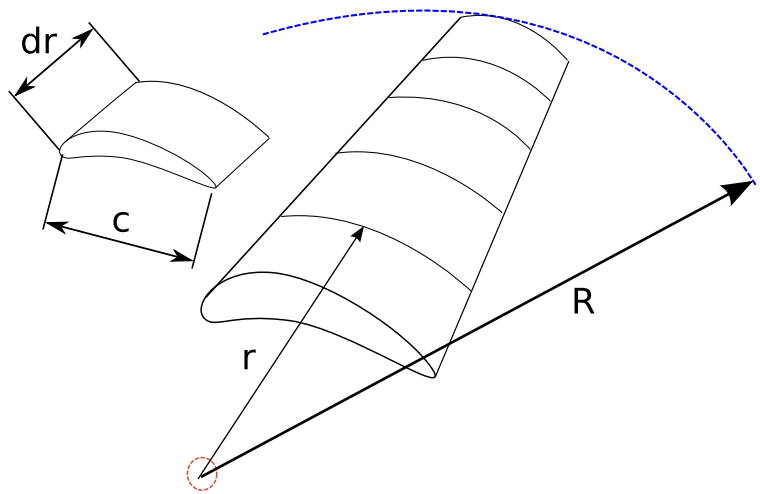

(b) Schematic of blade elements [7].

Governing Equations for BEM Used with AD Model I

$$S_{AD_x} = \frac{\rho V_{rel}^2 Bc}{4\pi rt} \left(C_l \cos\varphi + C_d \sin\varphi\right) \tag{4}$$

$$S_{AD_y} = \frac{\rho V_{rel}^2 Bc}{4\pi rt} \left(C_l \sin\varphi - C_d \cos\varphi\right) \cos\theta \tag{5}$$

$$S_{AD_z} = \frac{\rho V_{rel}^2 Bc}{4\pi rt} \left(C_l \sin\varphi - C_d \cos\varphi\right) \sin\theta \tag{6}$$

$$V_{rel} = \sqrt{(r\Omega + v\cos\theta - w\sin\theta)^2 + u^2}, \ \phi = \tan^{-1}\left(u/V_{rel}\right) \tag{7}$$

$$F_{tip} = \frac{2}{\pi}\cos^{-1} e^{-f}, f = \frac{B}{2}\frac{R-r}{R\sin\varphi} \tag{8}$$

$$F_{hub} = \frac{2}{\pi}\cos^{-1} e^{-f}, f = \frac{B}{2}\frac{r-r_{hub}}{r_{hub}\sin\varphi} \tag{9}$$

Governing Equations for BEM Used with AD Model II

The incompressible (RANS) equations are taken as the governing flow equations.

- The continuity equation:

$$\frac{\partial \overline{u}_i}{\partial x_i} = 0 \tag{10}$$

- The momentum equation:

$$\overline{u}_j \frac{\partial \overline{u}_i}{\partial x_j} = -\frac{1}{\rho}\frac{\partial \overline{p}}{\partial x_i} + \nu \frac{\partial^2 \overline{u}_i}{\partial x_j^2} - \frac{\partial \overline{u_i' u_j'}}{\partial x_j} + \frac{\vec{S}_{AD}}{\rho} \tag{11}$$

Verification and Validation of the Solver I

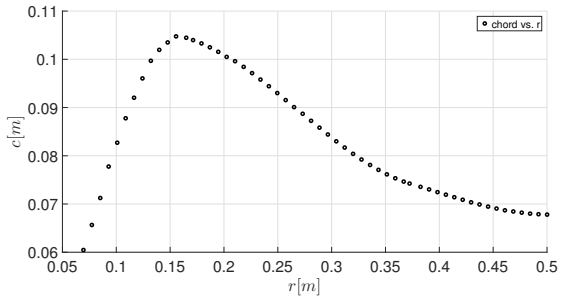

(a) Chord distribution.

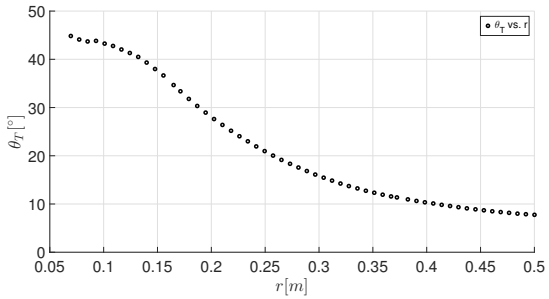

(b) Twist distribution.

Figure 11 : Chord and twist distribution of the blade given in table 7.

Table 7 : Airfoils along blade used in Ohya et al.[2, 4].

Radius	Airfoil Type
69.5mm	MEL20
357.0mm	MEL18
500.0mm	MEL12

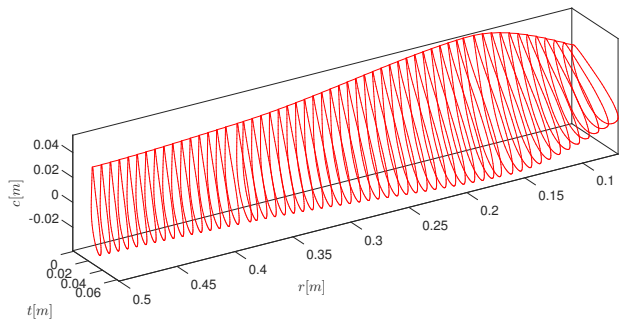

Figure 12 : Schematic diagram of the blade.

Verification and Validation of the Solver II

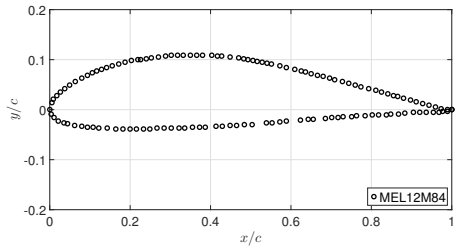

(a) MEL12M84.

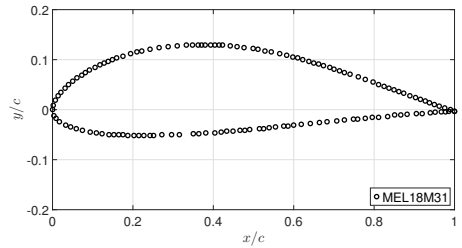

(b) MEL18M31.

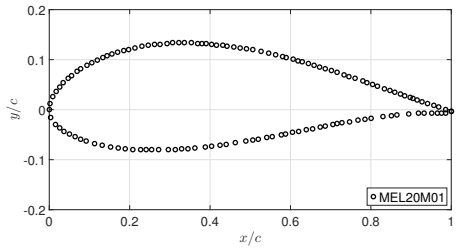

(c) MEL20M01.

Figure 13 : MEL airfoil series used in the blade [8].

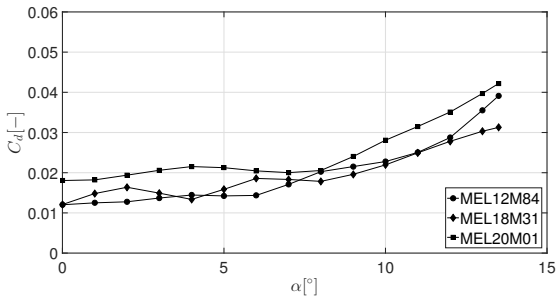

(a) Cd vs α distribution.

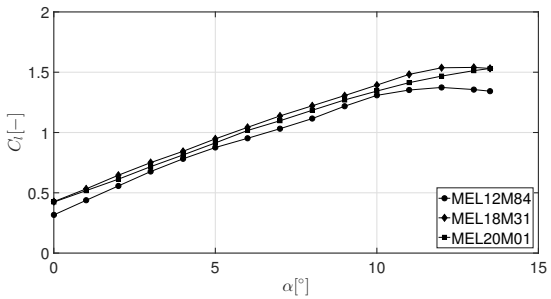

(b) Cl vs α distribution.

Figure 14 : Experimental lift and drag coefficients vs. angle of attack of each airfoil used in the blade [4].

Verification and Validation of the Solver III

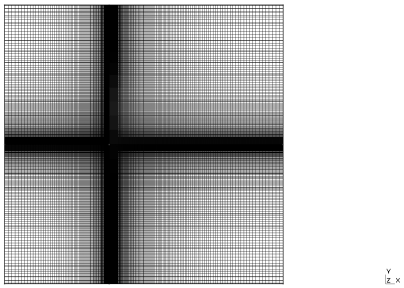

(a) Side view of the coarse grid.

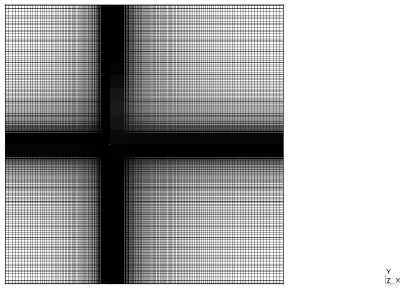

(b) Side view of the medium grid.

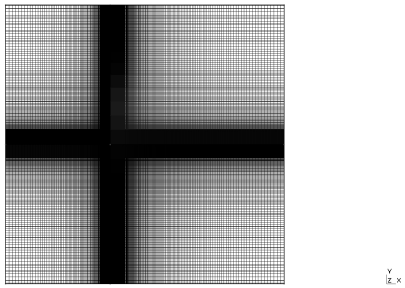

(c) Side view of the fine grid.

Figure 15 : Grids employed for the grid dependence study.

Table 8 : Results of three selected grids for tip speed $\lambda = 3.5$.

N_{nodes}	**Thrust [N]**	**Torque [N.m]**
148800	18.4465	1.80107
312768	18.1198	1.78795
536272	17.8072	1.77792

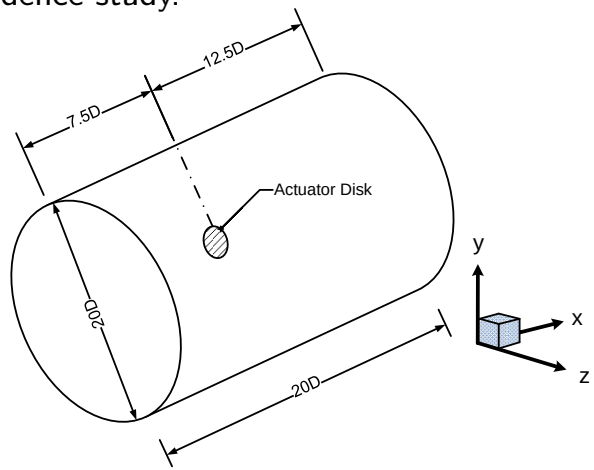

Figure 16 : Far-field domain used for simulation.

Verification and Validation of the Solver IV

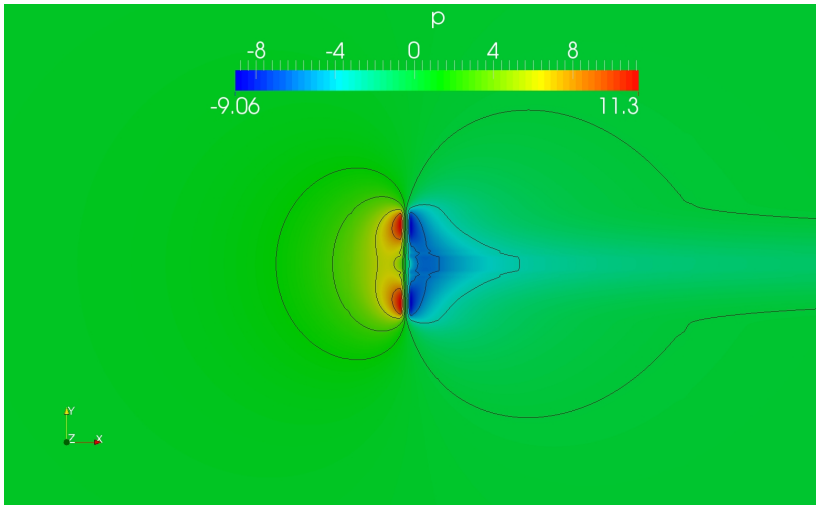

(a) Pressure distribution on the fine grid.

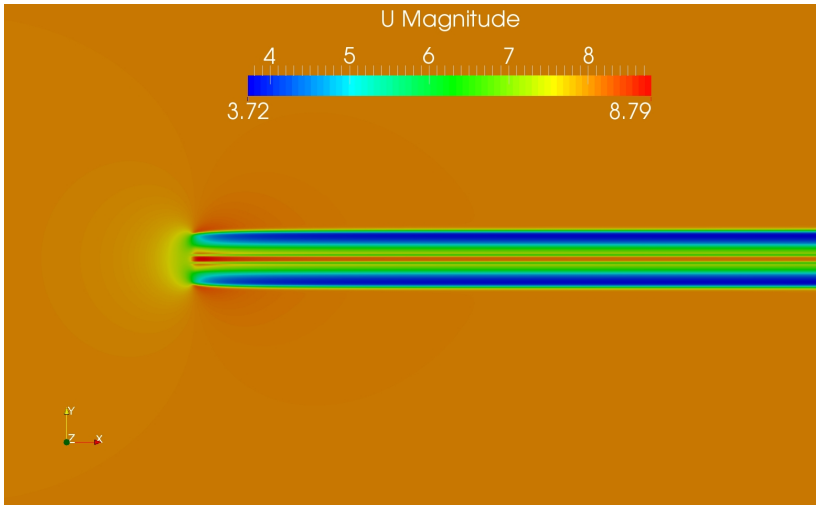

(b) Velocity distribution on the fine grid.

Figure 17 : Velocity and pressure distribution of the three grids for tip speed $\lambda = 3.5$.

Verification and Validation of the Solver V

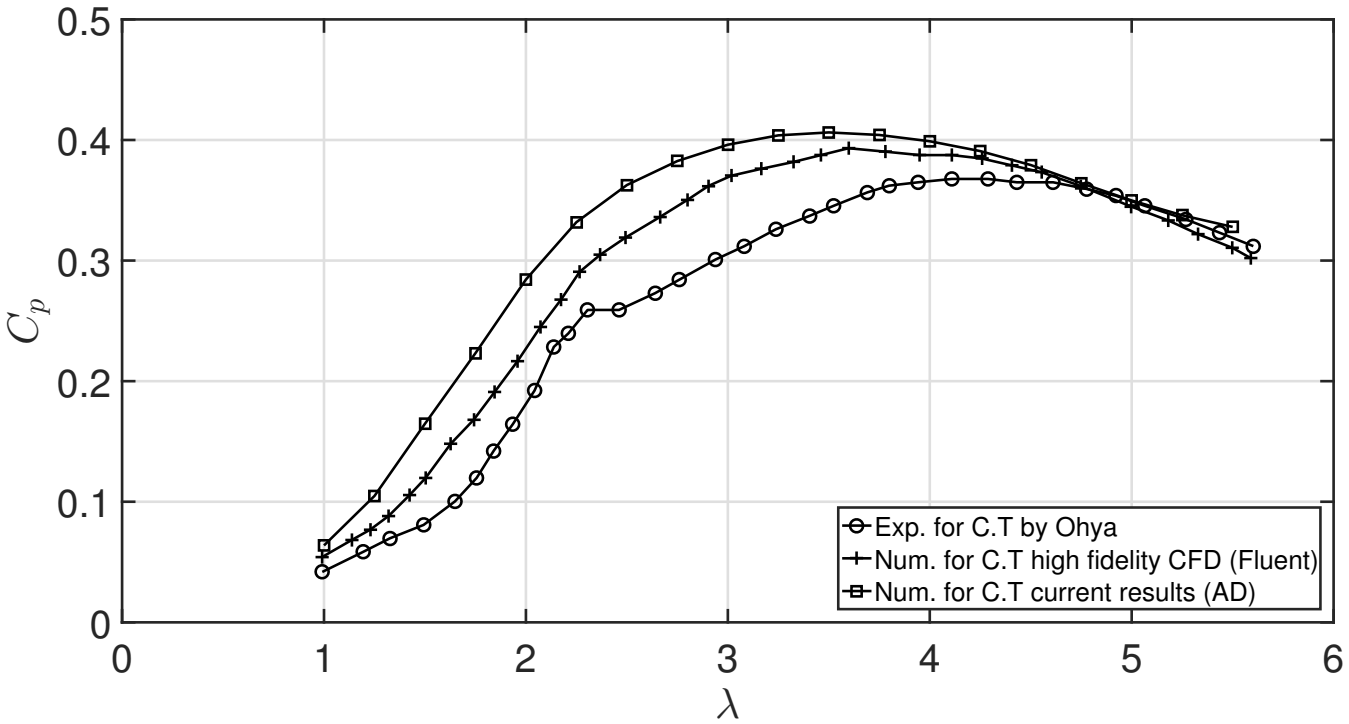

Figure 18 : Validation study of the power coefficients vs. tip speed [2, 4].

3D Vs. Axisymmetric Actuator Disk

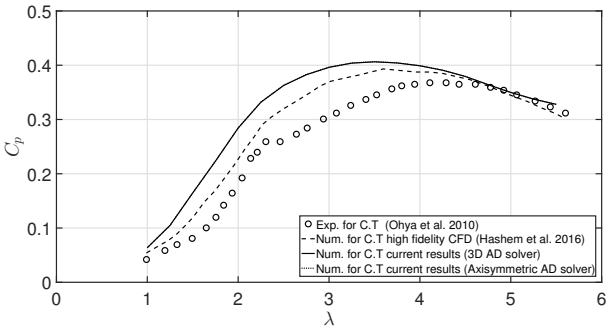

(a) Conventional turbine.

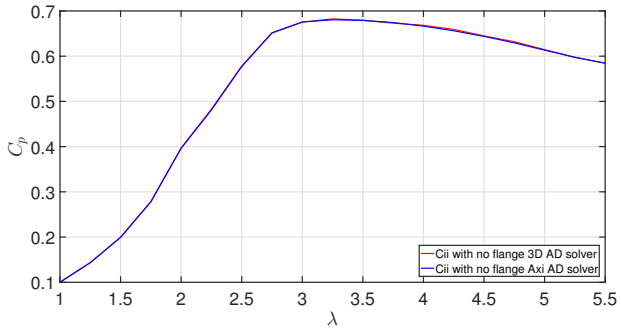

(b) Shrouded turbine.

Figure 19 : Verification of the axisymmetric implementation in comparison to full 3D and literature results.

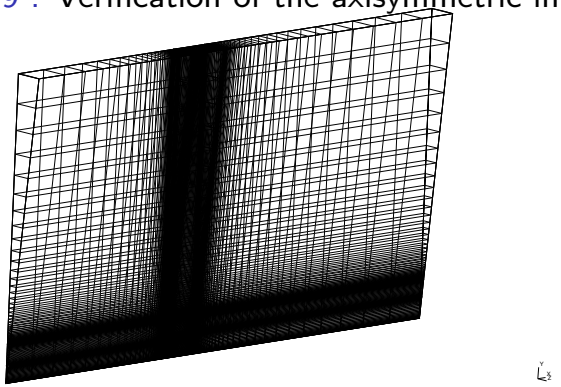

Figure 20 : Example of the axisymmetric grid.

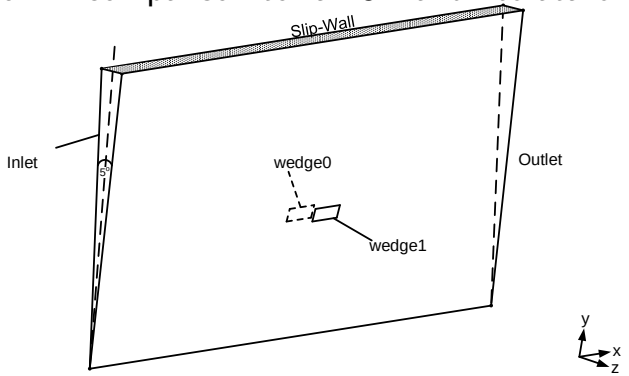

Figure 21 : Wedge boundary condition.

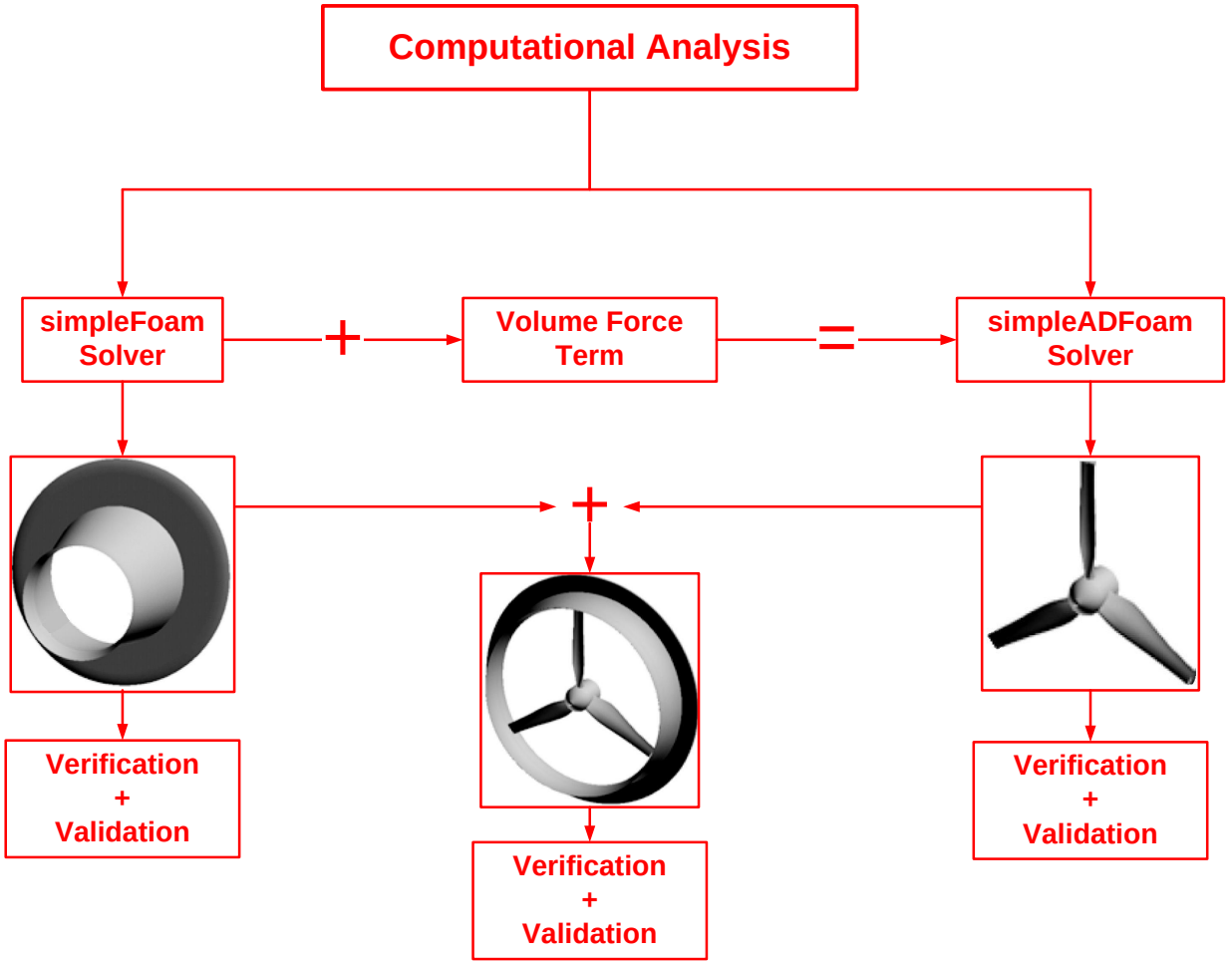
Computational Analysis
simpleFoam Solver
+
Volume Force Term
=
simpleADFoam Solver
+
Verification + Validation
Verification + Validation
Verification + Validation

Case Setup and Boundary Conditions I

Figure 24 : Detailed information of Cii-type wind-lens.

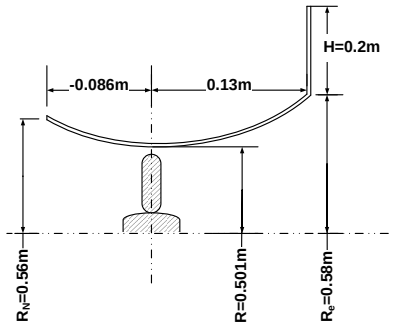

Table 9 : Fluid Properties.

Property	Value
Kinematic Viscosity ν	$1.5 \times 10^{-5} m^2/s^2$
Air Density ρ	$1.225 kg/m^3$
Reynolds No. Re	5.4×10^5

Table 10 : Pertinent discretization information.

Aspect	Description
Coordinates system	Axisymmetric
Computational grid	5° wedge
Scheme	Finite volume method
Coupling algorithm	SIMPLE method
Laplacian schemes	Gauss limitedLinear
Gradient schemes	cellLimited $<$ *gradScheme* $>$
Divergence schemes	upwind

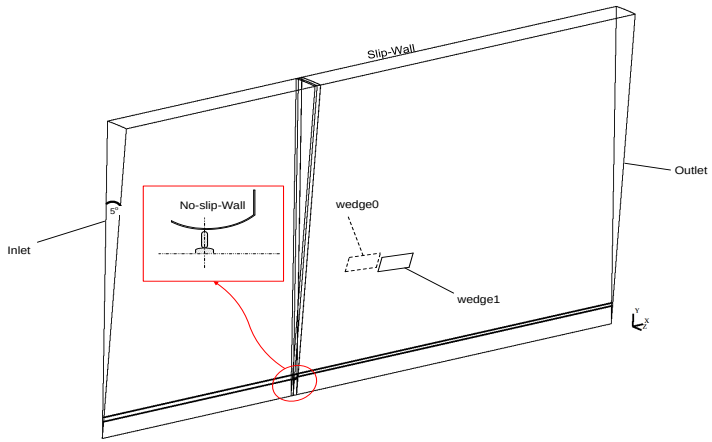

Figure 22 : Computational domain and BCs.

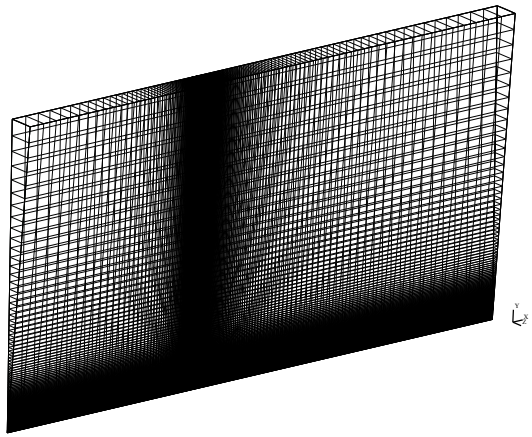

Figure 23 : Example of the axisymmetric grid.

Case Setup and Boundary Conditions II

- Computational domain: Axisymmetric (length = 20D, Diameter=10D)
- Fluid is set to be air at a temperature of $25^{\circ}C$.
- Reference pressure: 1 atm.
- Turbulent inflow: $I_0 = 3.1\%$, $k_0 = 0.09m^2/s^2$ and $\epsilon_0 = 0.063m^2$
- Pressure outlet: 0 Pa
- Domain walls: free slip wall
- Diffuser walls: no slip walls with $k_{wall} = \epsilon_{wall} = 0$.

Table 11 : Conditions employed for all designs in the optimization process.

Parameter	**Value**
Number of blades N	3
Rotational Speed Ω	535 rpm
Tip speed ratio λ	3.5
Rotor tip radius R_{tip}	0.5 m
Hub radius R_{hub}	0.065 m
Rotor tip clearance	10 mm
Velocity inlet	8 m/s
Blade element profile	MEL12, MEL18, and MEL20

Effect of Turbulence Models I

(a) $k-\epsilon$ model. (b) $k-\omega$ SST model. (c) $S-A$ model.

Figure 25 : Streamline distributions for the *Cii*-type shroud using different turbulent models with and without turbine at a tip speed of $\lambda = 3.5$.

Table 12 : The effect of turbulent models on the thrust and power coefficients at tip speed of $\lambda = 3.5$.

Quantity	$k-\omega$ *SST*	$k-\epsilon$	$S-A$
C_P	0.8320	0.8725	0.9066
C_t	0.9078	0.9297	0.9501

Effect of Turbulence Models II

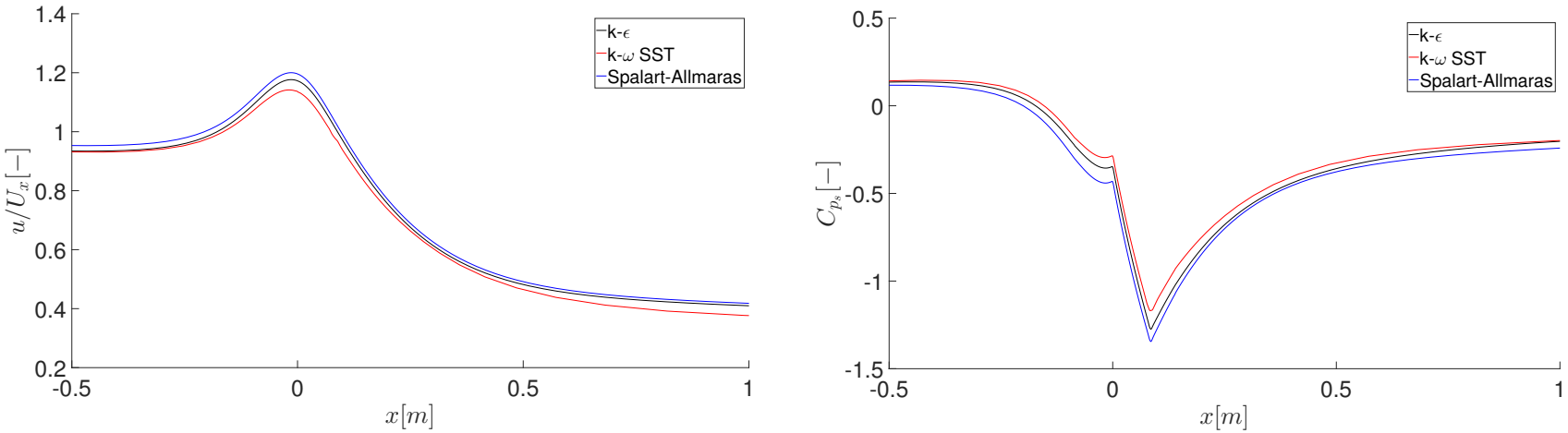

(a) Velocity distribution.

(b) Pressure distribution.

Figure 26 : Velocity and pressure distribution through an empty flanged diffuser using different turbulence models.

Conclusion

Even though the $k-\omega$ (SST) turbulence model results are in best agreement due to its ability to model boundary layer separation in adverse pressure gradients, it is not always practical to mesh down to $y^+ \simeq 1$ wall spacings when considering the overall computational cost required to search for an optimized shrouded design in the preliminary design stage. Therefore, the $k-\epsilon$ with standard wall functions is chosen.

Full Configuration I

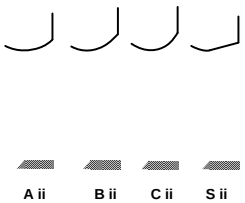

Figure 27 : Sectional shapes of wind-lenses used by Ohya et al.[2].

Table 13 : Parameters for wind-lens shapes by Ohya et al.[2].

Diffuser	A ii	B ii	C ii	S ii
$(L_D + L_N)/D$	0.225	0.221	0.221	0.225
A_{exit}/A_{throat}	1.173	1.288	1.294	1.119

Table 14 : Detailed information for Sii-types wind-lens.

Experimental model	Compact Sii type
Diameter of the throat D	1020mm
Diameter of the hub D_h	0.13D
Height of the flange h	0.1D
Diffuser length L_D	0.137D
Inlet length L_N	0.088D
Tip clearance	10 mm
Semi-open angle θ	12^o
Inlet velocity V_∞	8 m/s

Full Configuration II

Figure 28 : Comparisons among low- and high-fidelity CFD results as well as experimental data.

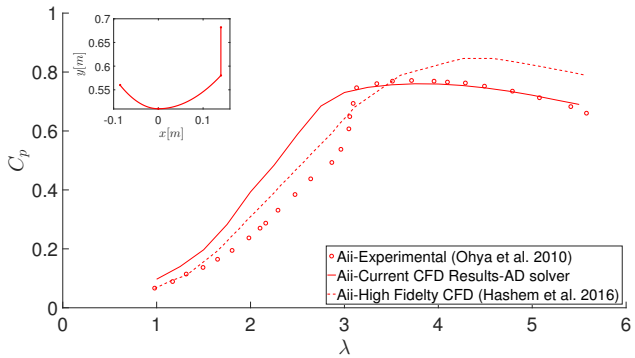

(a) *Aii* Type.

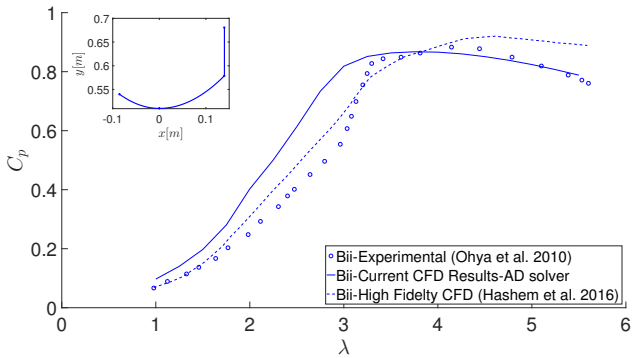

(b) *Bii* Type.

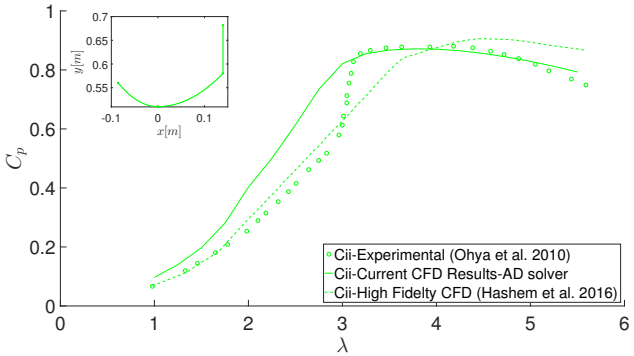

(c) *Cii* Type.

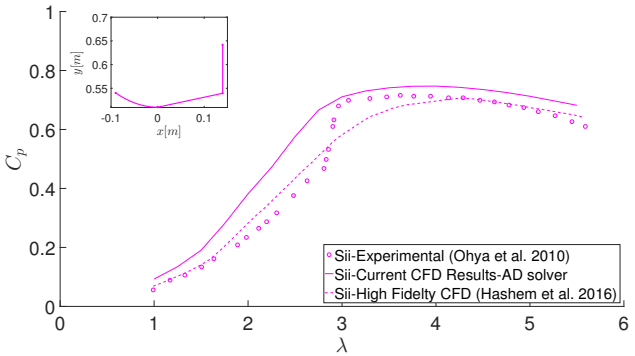

(d) *Sii* Type.

Optimization Algorithm

- One popular approach for optimization processes is evolutionary algorithms specifically, the use of Genetic Algorithms (GAs).
- GAs are semi-stochastic semi-deterministic optimization methods presented as natural evolution.
- GAs are based on the evaluation of a set of solutions (population).
- Random operations of selection, crossover and mutation are applied to the population.
- The probability of survival of new individuals relies on their fitness: the best are kept with a high probability, the worst are rapidly discarded [9].
- In this work, the software package DAKOTA with MOGA (Multi-Objective Genetic Algorithm) [10] is employed.

Why is a derivative-free global optimization method chosen?

This multi-objective shape optimization problem exhibits multimodal behavior and we do not have adjoint gradients available.

Shape Parameterization I

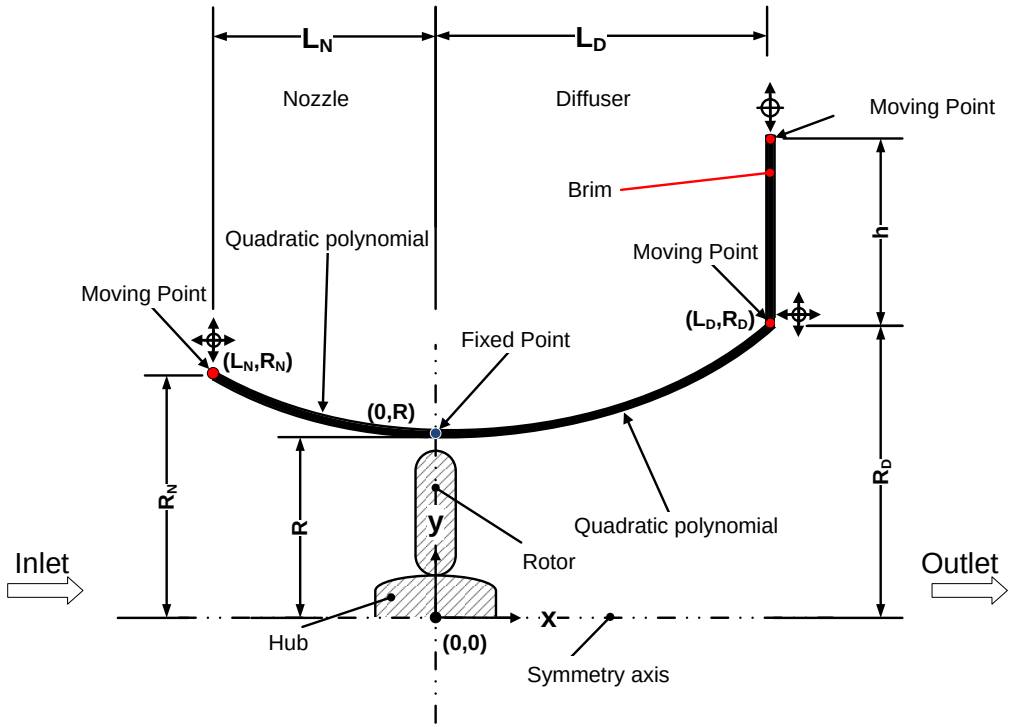

Figure 29 : Five design variables for the parameterization.

5 Design variables for the *Cii* type wind-lens

Nozzle length and diameter, diffuser length and diameter as well as the flange height in the y direction.

Shape Parameterization I

Shape Parameterization II

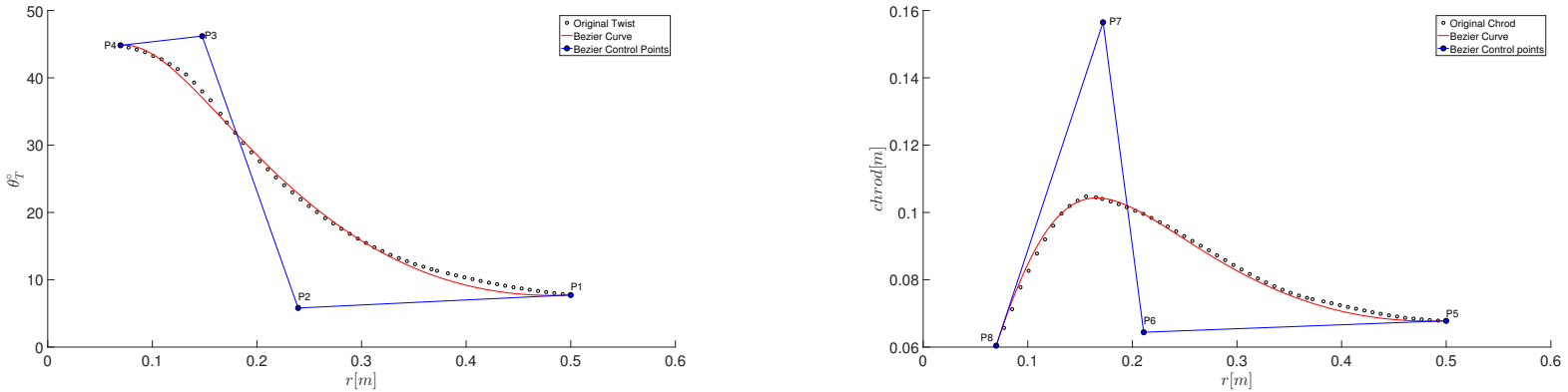

(a) Twist distribution.

(b) Chord distribution.

Figure 30 : Bezier curves and their control points for the original twist and chord distributions.

Table 15 : Range of twist and chord distribution variables.

Control Point	P_1	P_2	P_3	P_4	P_5	P_6	P_7	P_8
Original value x	0.500	0.239	0.148	0.0695	0.5000	0.2108	0.1720	0.0698
Original value y	7.743	5.800	46.200	44.818	0.0678	0.0664	0.1565	0.0604
max y	-	-	50.000	50.000	-	-	0.10	-
min y	-	-	30.000	40.000	-	-	0.18	-

Shape Parameterization II

Objective Functions

- This work focuses on the shape optimization of the wind-lens for a given wind turbine rotor in order to maximize the power coefficient, C_P, while at the same time minimizing the drag and thrust.
- The thrust coefficient, C_t, of the turbine is determined by integrating the axial force over the blade.
- The power coefficient, C_P, of the turbine is determined by integrating the radial and tangential forces over the blade.
- The drag coefficient, $C_d = \dfrac{F_d}{0.5\rho V_\infty^2 A_{brim}}$, is calculated using the force function in **OpenFOAM**.

Summary of Optimization Framework

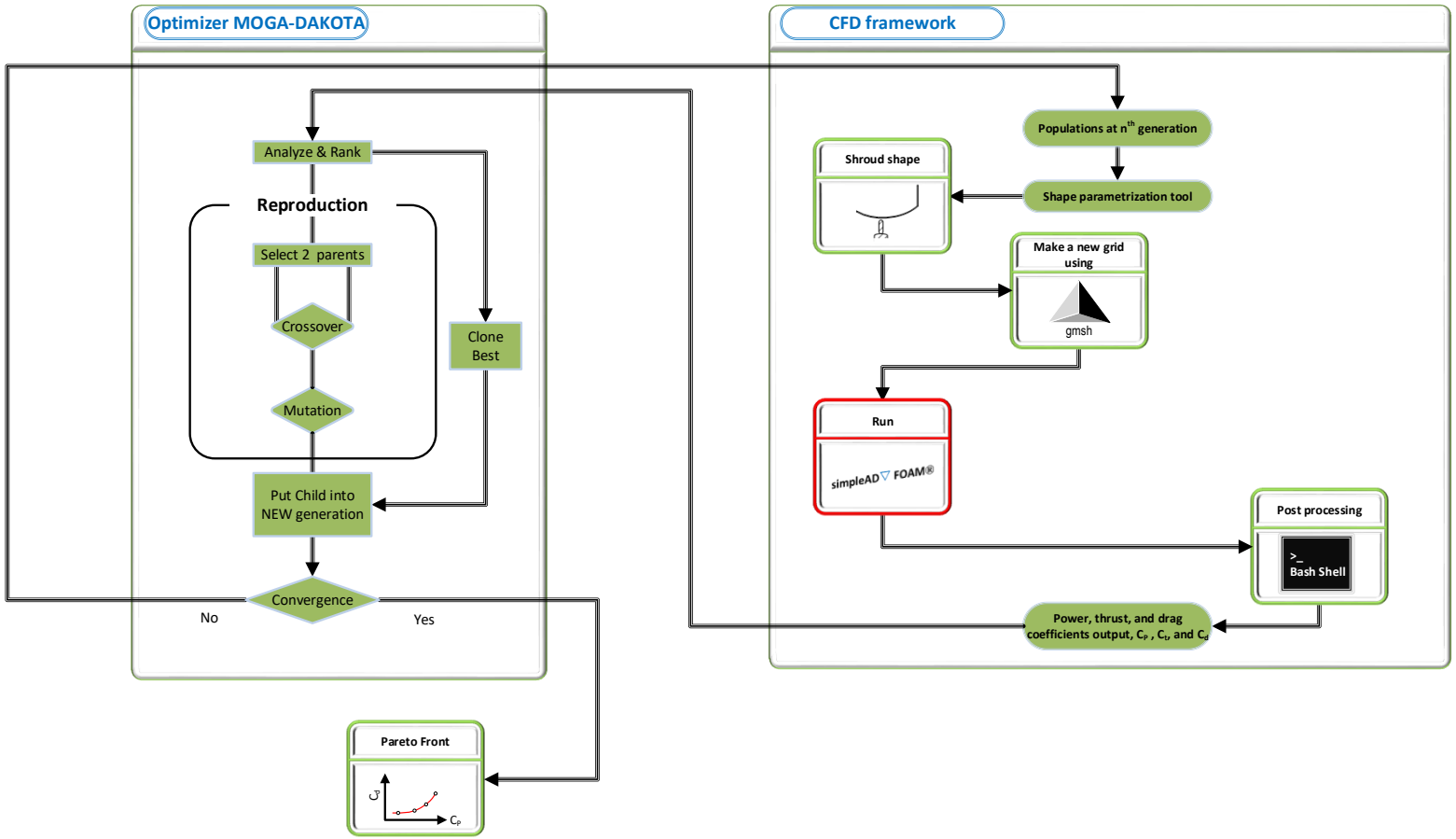

Figure 31 : Flow chart of the optimization approach.

Case Setup I

Table 16 : Conditions employed for all designs in the optimization process.

Parameter	Value
Number of blades N	3
Rotational Speed Ω	535 rpm
Tip speed ratio λ	3.5
Rotor tip radius R_{tip}	0.5 m
Hub radius R_{hub}	0.065 m
Rotor tip clearance	10 mm
Velocity inlet	8 m/s
Blade element profile	MEL12, MEL18, and MEL20

- Computational domain: Axisymmetric (length = 20D, Diameter=10D)
- Fluid is set to be air at a temperature of $25^{\circ}C$.
- Reference pressure: 1 atm.
- Turbulent inflow: $I_0 = 3.1\%$, $k_0 = 0.09m^2/s^2$ and $\epsilon_0 = 0.063m^2$
- Pressure outlet: 0 Pa
- Domain walls: free slip wall
- Diffuser walls: no slip walls with $k_{wall} = \epsilon_{wall} = 0$.

Case Setup II

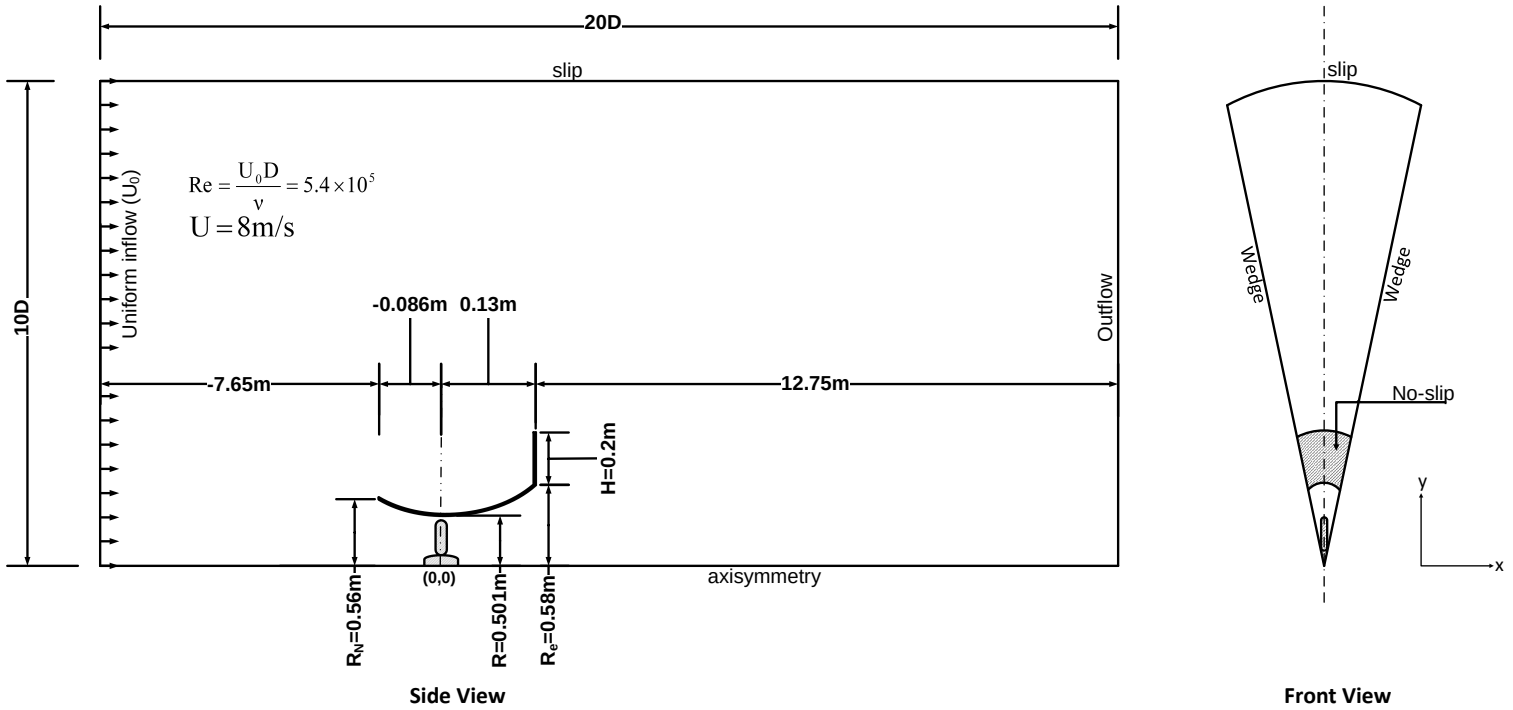

Figure 32 : CFD domain used for simulation.

Case Setup III

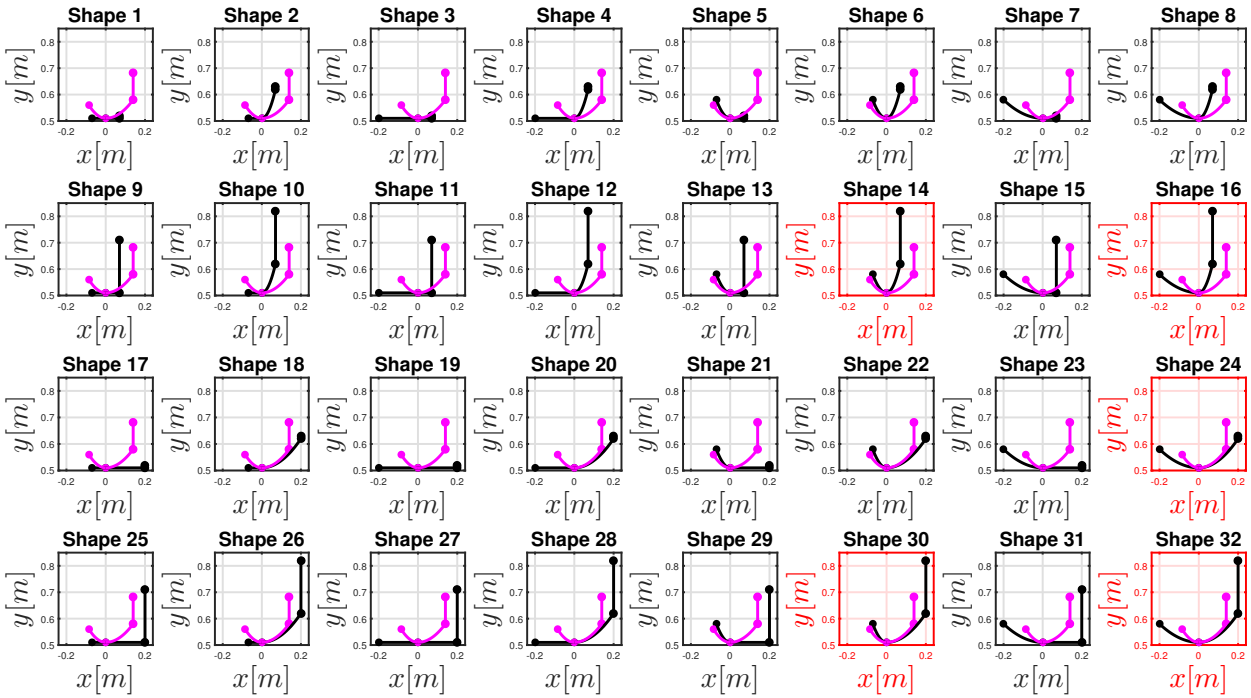

Figure 33 : $2^5 = 32$ extreme shapes in design space.

Sample Grid Convergence Study

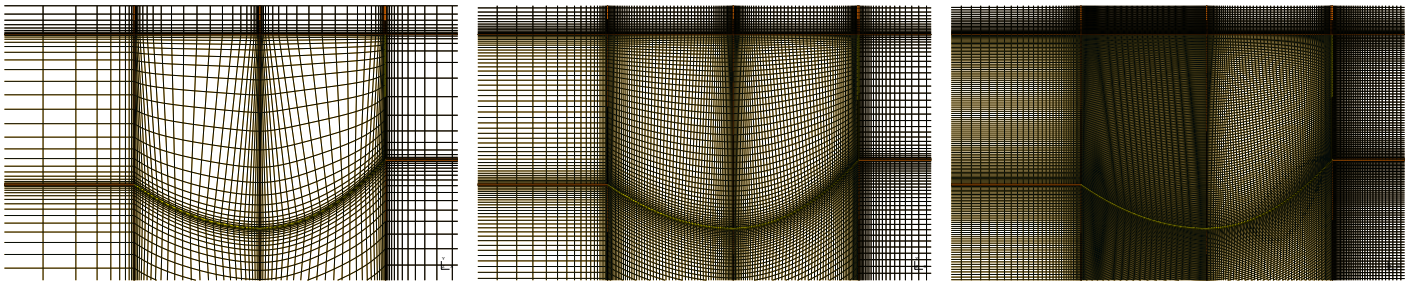

(a) Coarse Grid. (b) Medium Grid. (c) Fine Grid.

Figure 34 : Three grids employed for grid convergence study for shape 32.

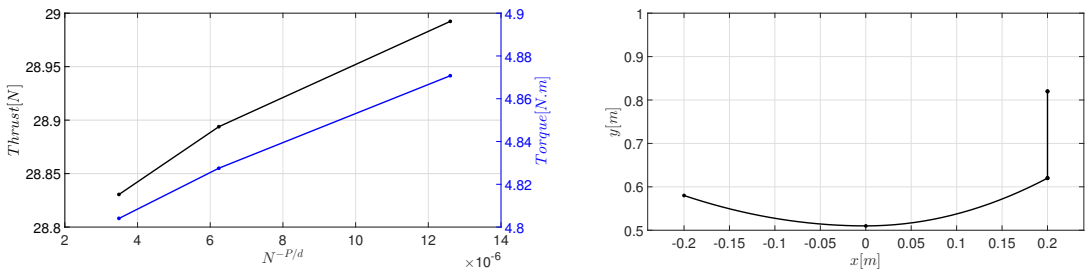

(a) Thrust and torque - Profile 32. (b) Profile 32.

Figure 35 : Grid convergence studies of thrust and torque w.r.t. number of nodes for profile 32.

Verification via Inverse Design I

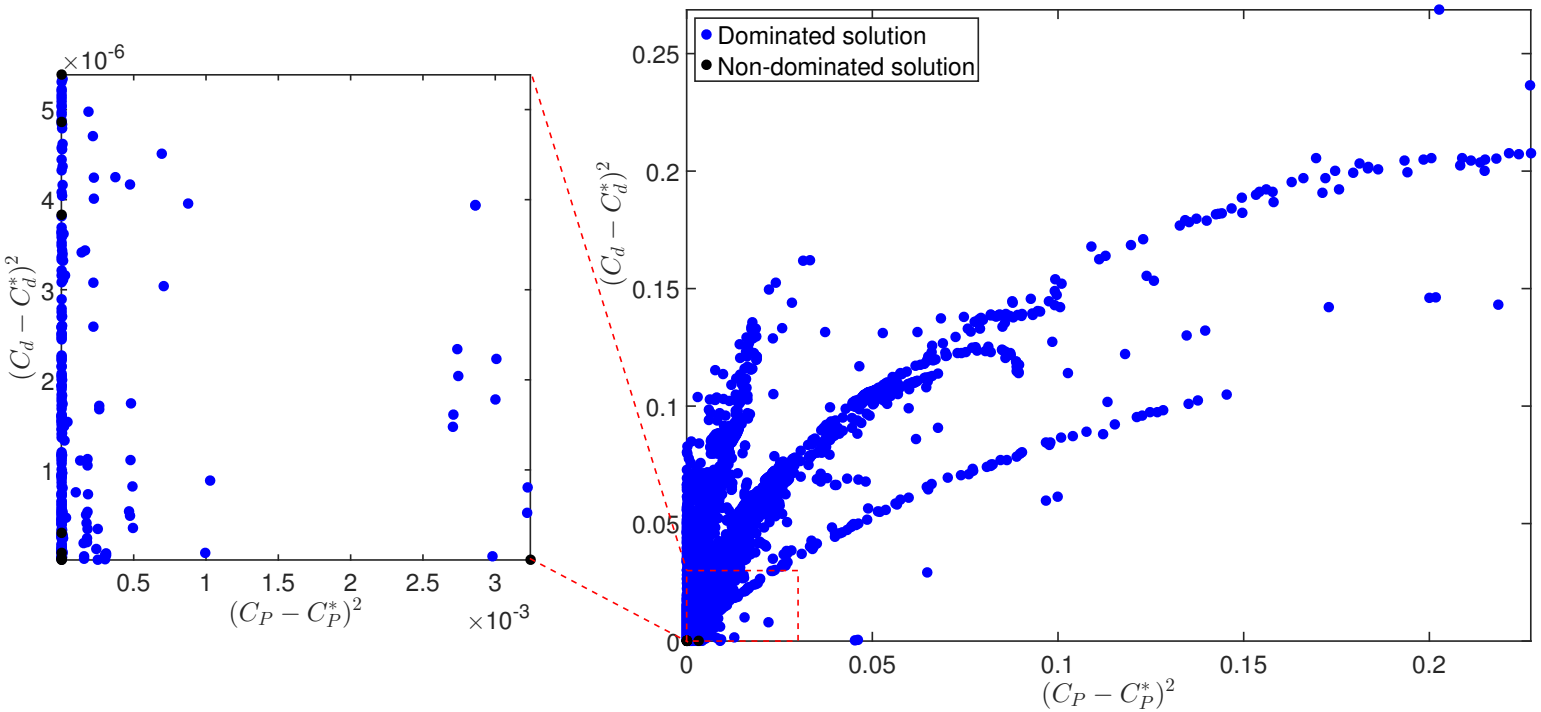

Figure 36 : Dominated and non-dominated solutions of an inverse design simulation.

Verification via Inverse Design II

Table 17 : Comparisons between the target and optimized profiles A, B, and C.

	L_D	h	R_N	L_N	R_D	$\left(C_P - C_P^*\right)^2$	$\left(C_d - C_d^*\right)^2$
Target Profile	0.174	0.02	0.536	0.181	0.604	0	0
Optimized Profile A	0.184	0.137	0.571	0.124	0.571	5.54×10^{-12}	5.39×10^{-06}
Optimized Profile B	0.189	0.046	0.535	0.089	0.587	5.31×10^{-09}	7.73×10^{-08}
Optimized Profile C	0.139	0.063	0.521	0.147	0.558	3.24×10^{-03}	1.72×10^{-10}

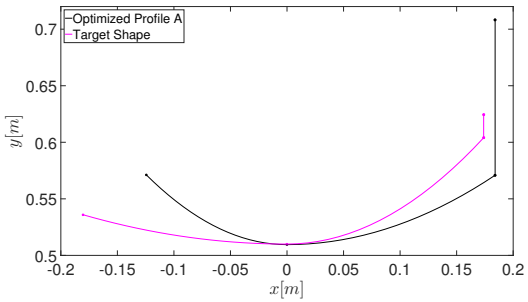

(a) Optimized shape A.

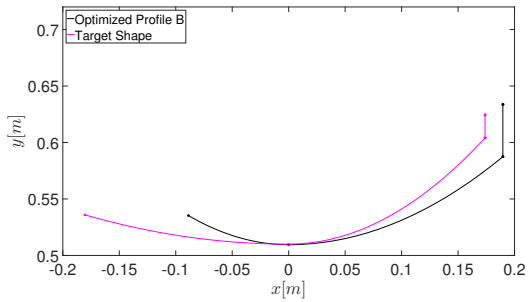

(b) Optimized shape B

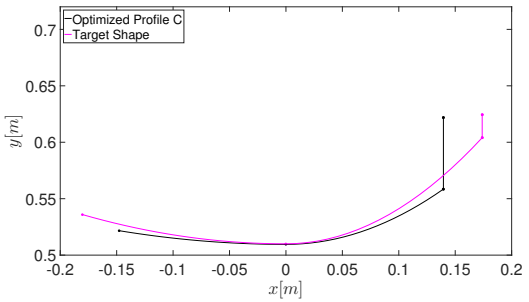

(c) Optimized shape C.

Figure 37 : Inverse design optimized shapes in comparison to target shape.

Case I - Shape Optimization Results I

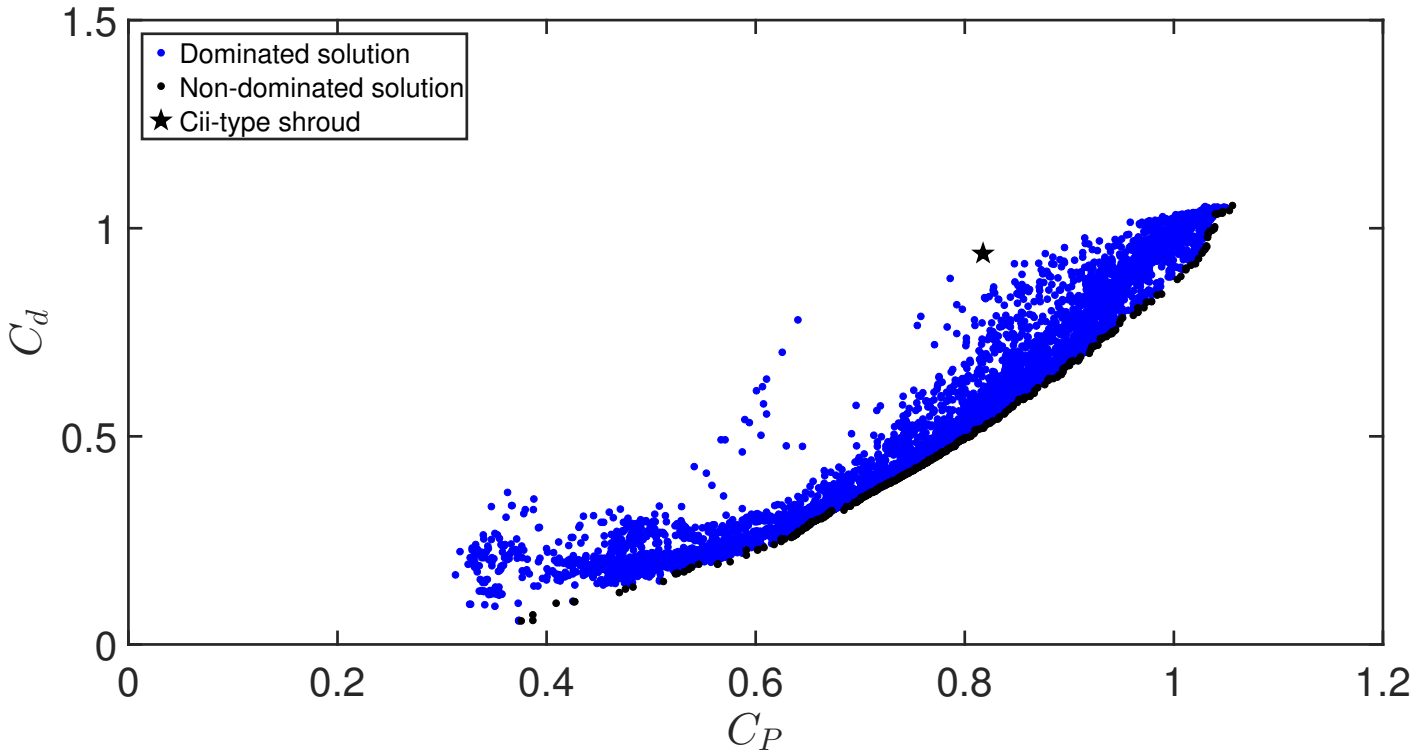

(a) Dominated vs. non-dominated solutions.

Figure 38 : Optimization results.

Case I - Shape Optimization Results II

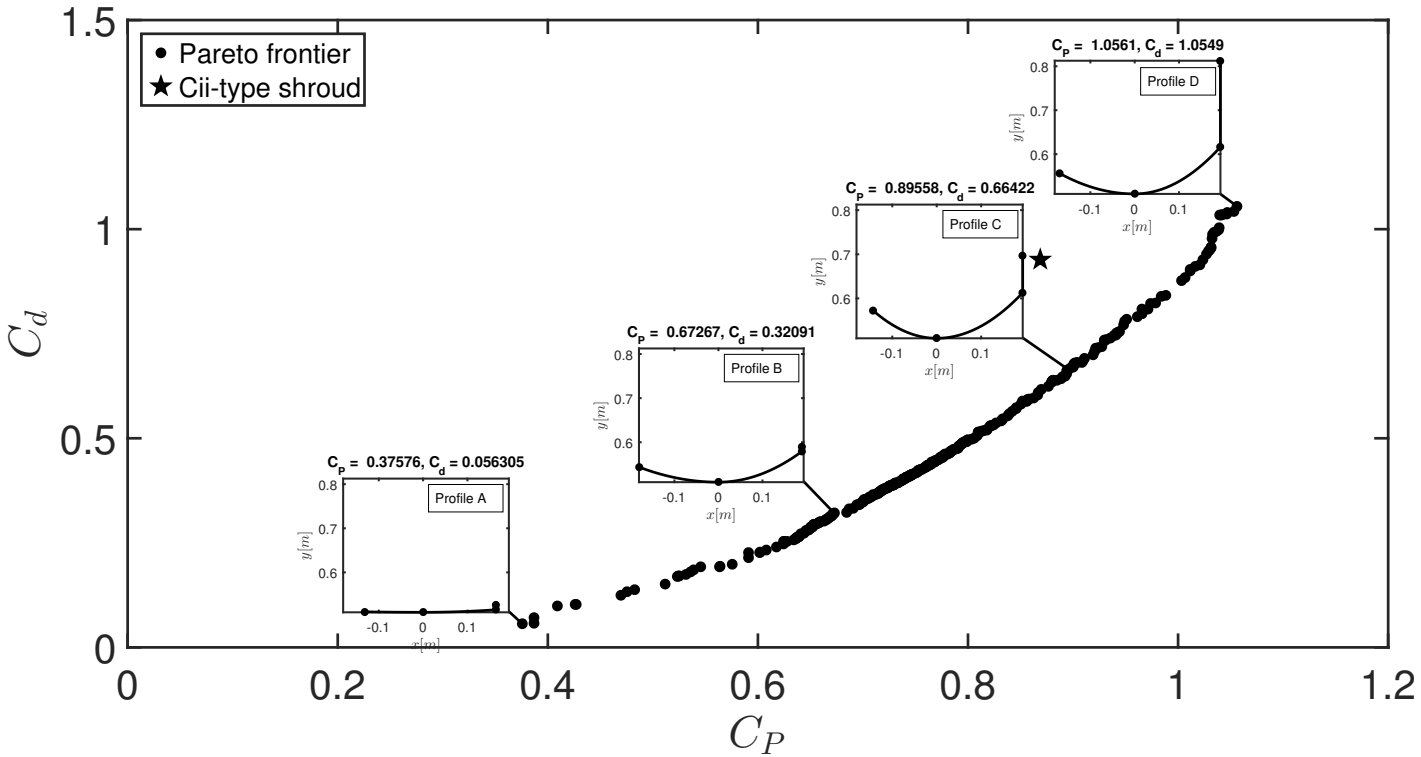

(b) Pareto frontier.

Figure 38 : *Cont.*

Case I - Shape Optimization Results III

Table 18 : Comparison between the *Cii* type shroud and optimized profiles C, D, and E.

	L_D	h	R_N	L_N	R_D	C_P	C_d
Cii shroud	0.139	0.102	0.550	0.0897	0.580	0.817	0.939
Profile *C*	0.193	0.084	0.573	0.143	0.613	0.896	0.664
Profile *D*	0.193	0.198	0.557	0.169	0.616	1.056	1.055
Profile *E*	0.193	0.161	0.577	0.176	0.616	1.003	0.876

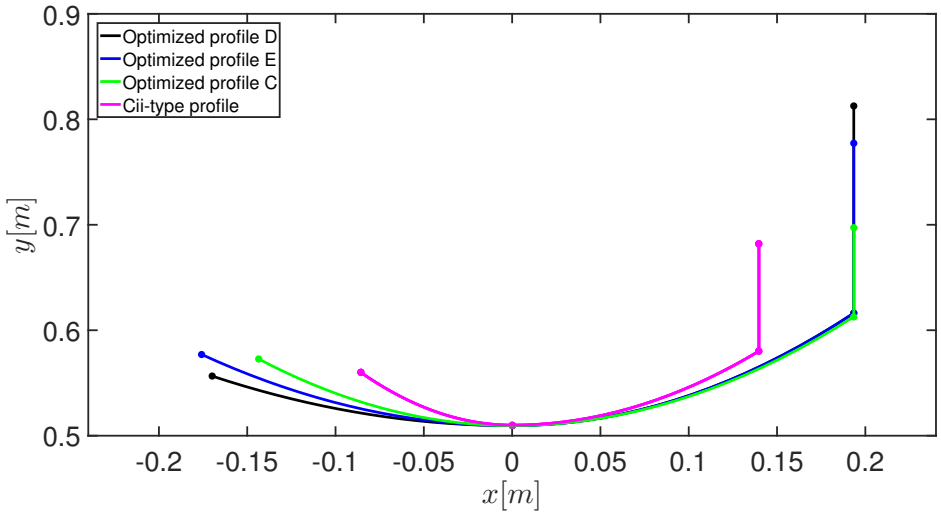

Figure 39 : Selected optimized profiles and baseline shape.

Case I - Shape Optimization Results IV

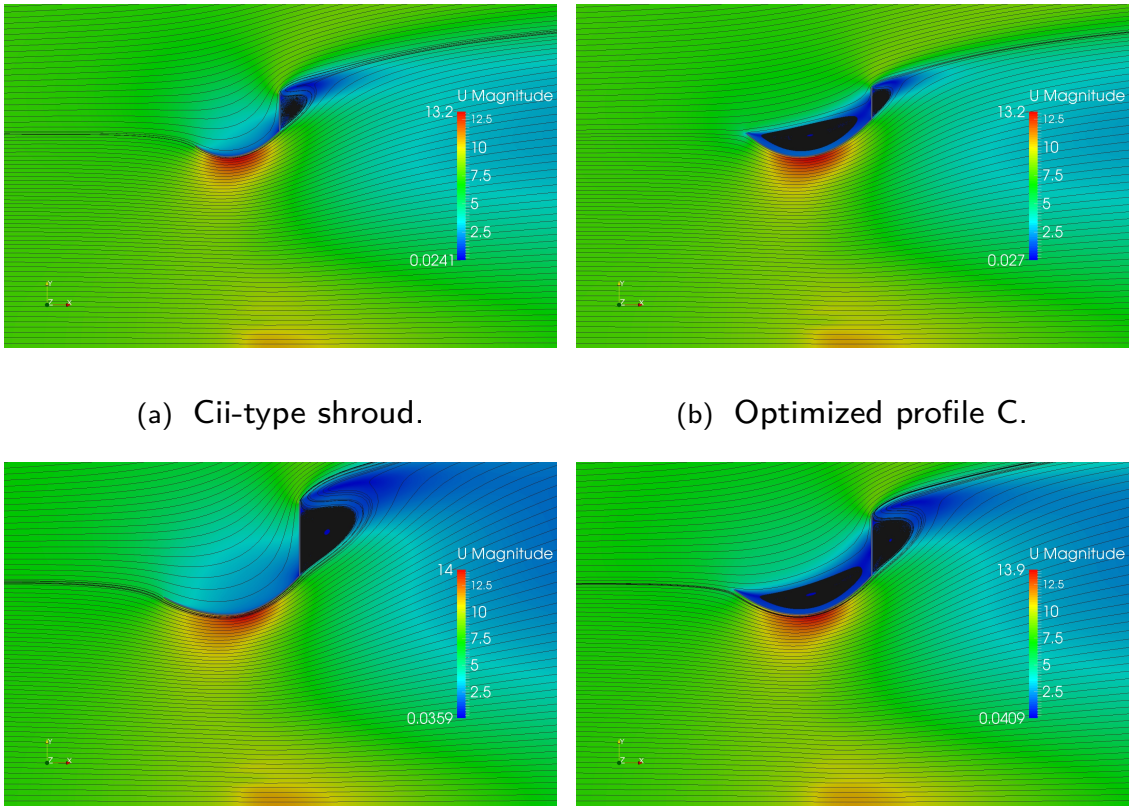

(a) Cii-type shroud.

(b) Optimized profile C.

(c) Optimized profile D.

(d) Optimized profile E.

Figure 40 : Velocity distribution with streamlines for *Cii* profile and optimized profiles C, D, and E.

Case II - Overview

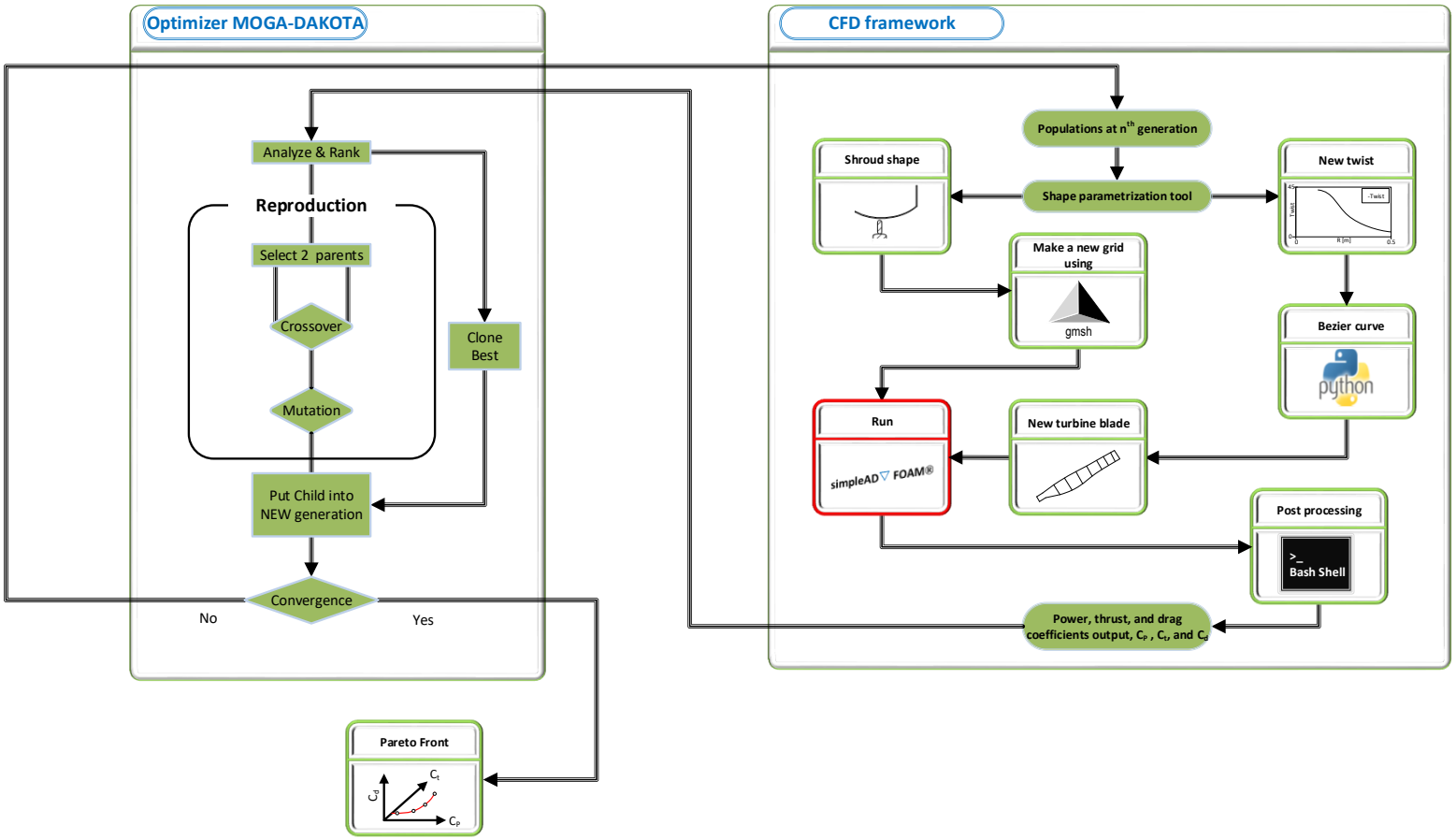

Figure 41 : Flow chart of the optimization approach.

Case II - Shape Optimization Results I

Case II - Shape Optimization Results II

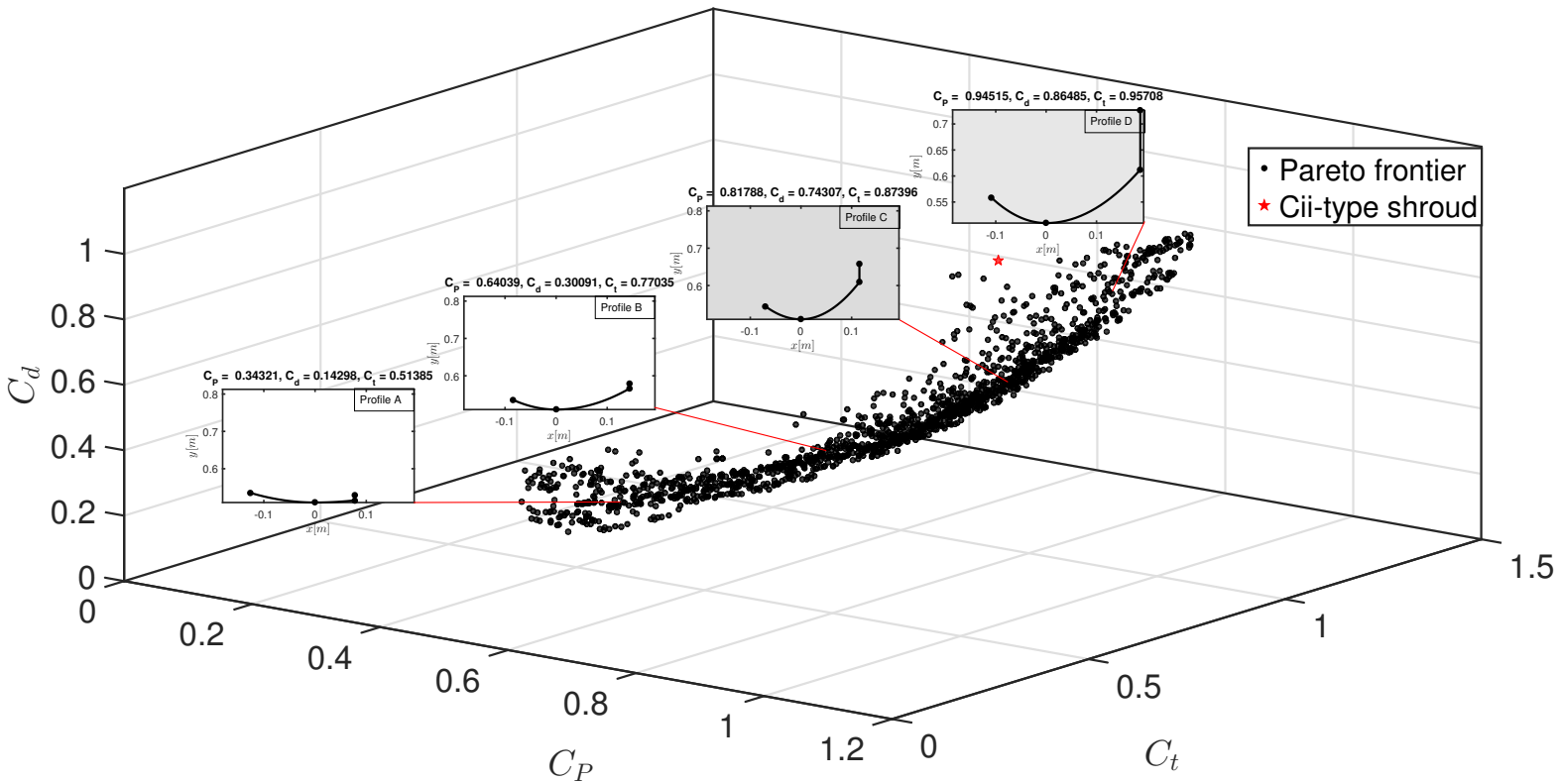

Figure 42 : Pareto frontier.

Case II - Shape Optimization Results III

Table 19 : Comparison between the *Cii* type shroud and optimized profiles C and D.

	L_D	h	R_N	L_N	R_D	C_P	C_d	C_t
Cii shroud	0.139	0.102	0.550	0.0897	0.580	0.817	0.939	0.8936
Profile *C*	0.115	0.048	0.544	0.0702	0.609	0.817	0.743	0.8744
Profile *D*	0.186	0.114	0.558	0.1091	0.612	0.954	0.864	0.9570

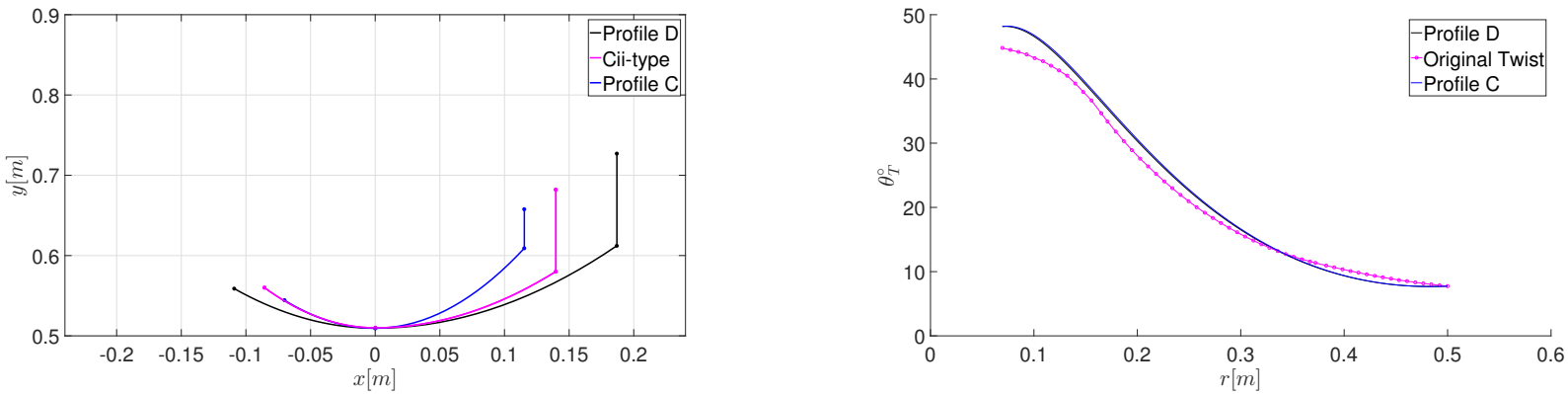

(a) Optimized profiles.

(b) Optimized twist.

Figure 43 : Selected optimized profiles and baseline shape.

Case II - Shape Optimization Results IV

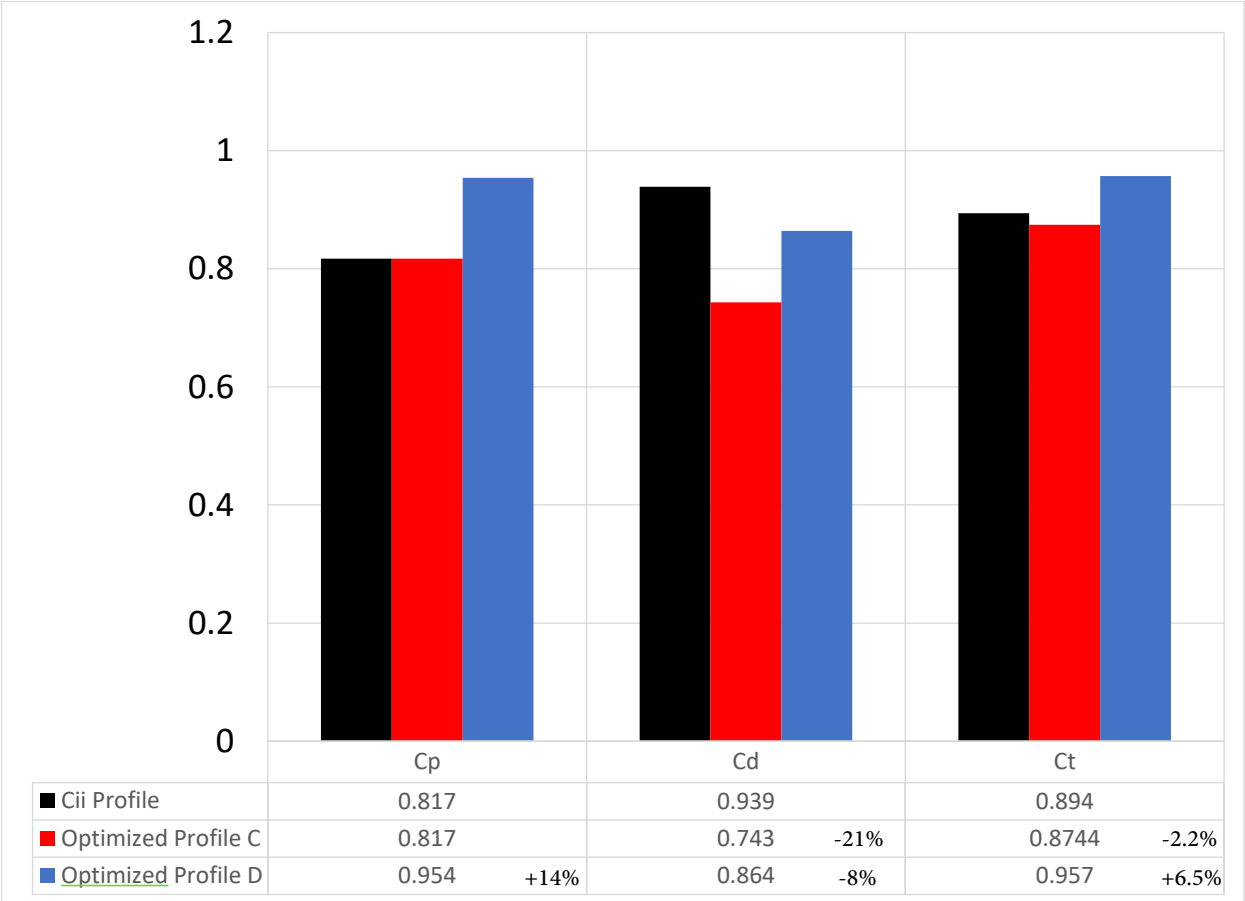

	Cp		Cd		Ct	
Cii Profile	0.817		0.939		0.894	
Optimized Profile C	0.817		0.743	-21%	0.8744	-2.2%
Optimized Profile D	0.954	+14%	0.864	-8%	0.957	+6.5%

Figure 44 : Summary of table 19.

Case II - Shape Optimization Results IV

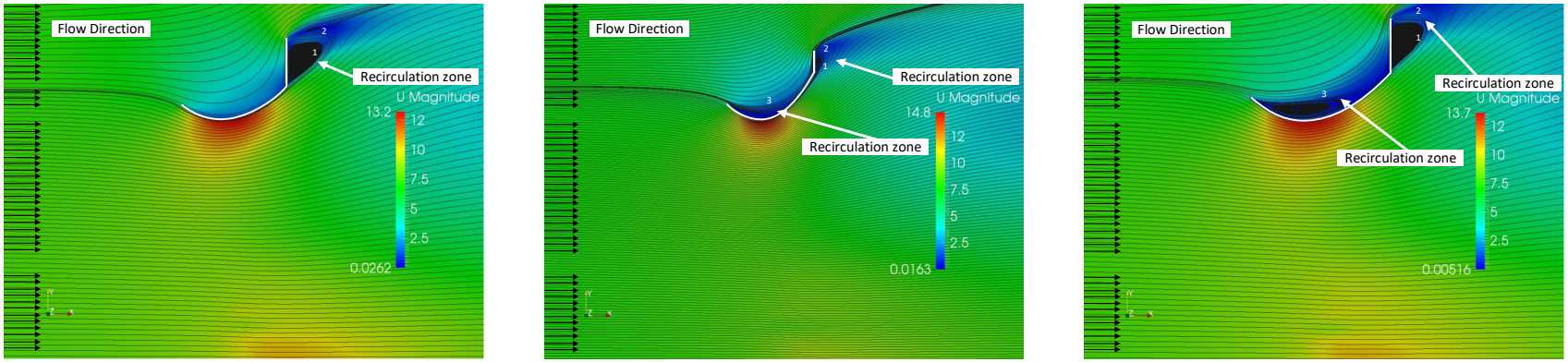

(a) Cii-type shroud. (b) Optimized profile C. (c) Optimized profile D.

Figure 45 : Velocity distribution with streamlines for *Cii* profile and optimized profiles C and D.

Case III - Overview

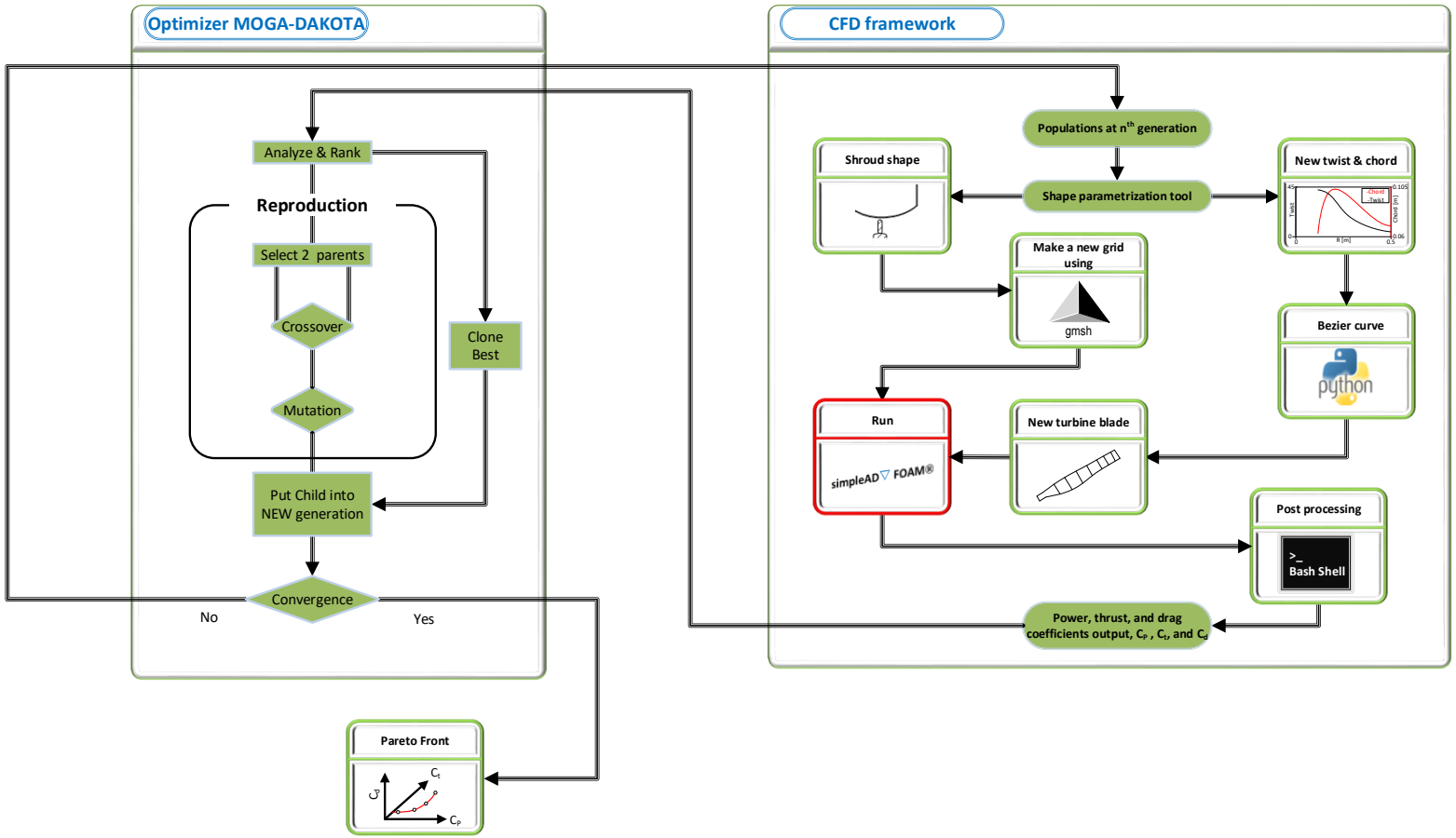

Figure 46 : Flow chart of the optimization approach.

Case III - Shape Optimization Results I

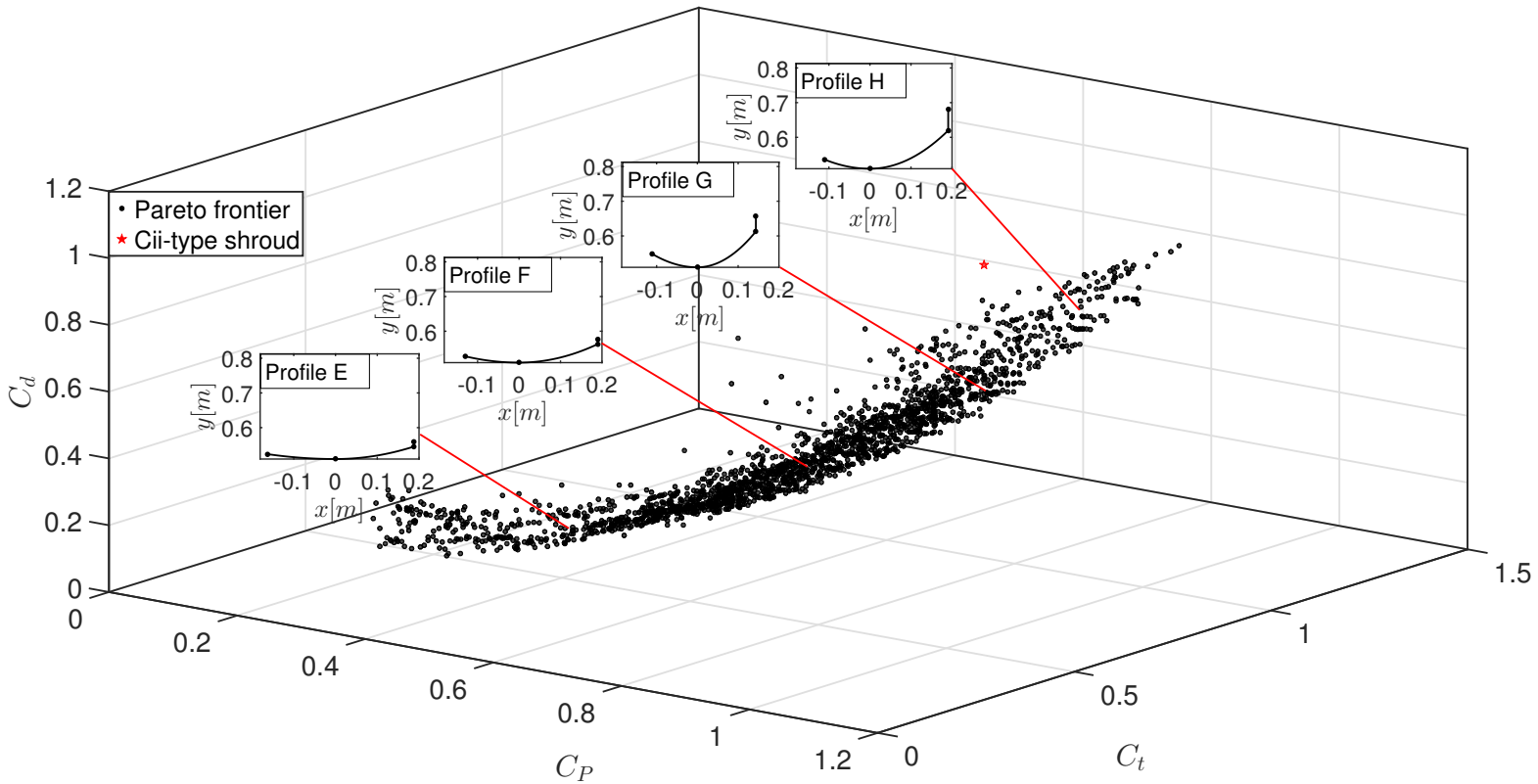

Figure 47 : Pareto frontier.

Case III - Shape Optimization Results II

Table 20 : Comparison between the *Cii*-type shroud and optimized profiles G and H.

	L_D	h	R_N	L_N	R_D	θ_P	C_P	C_d	C_t
Cii shroud	0.139	0.102	0.550	0.089	0.580	-2.300	0.817	0.939	0.894
Profile *G*	0.143	0.045	0.548	0.110	0.613	2.990	0.831	0.760	0.750
Profile *H*	0.190	0.061	0.536	0.110	0.619	3.212	0.923	0.845	0.816

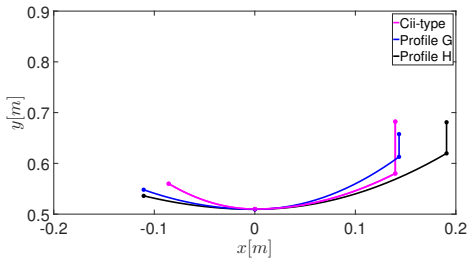

(a) Optimized profiles.

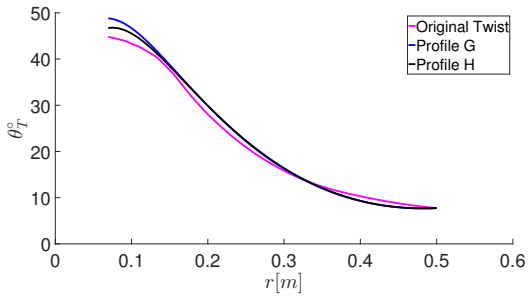

(b) Optimized twist.

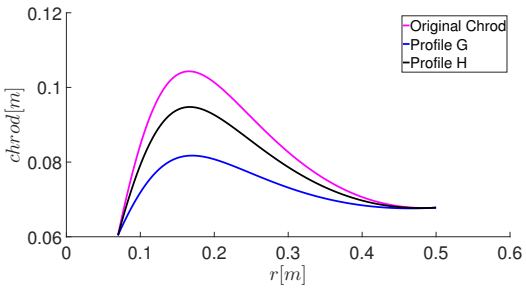

(c) Optimized chord.

Figure 48 : Selected optimized profiles and baseline shape.

Case III - Shape Optimization Results III

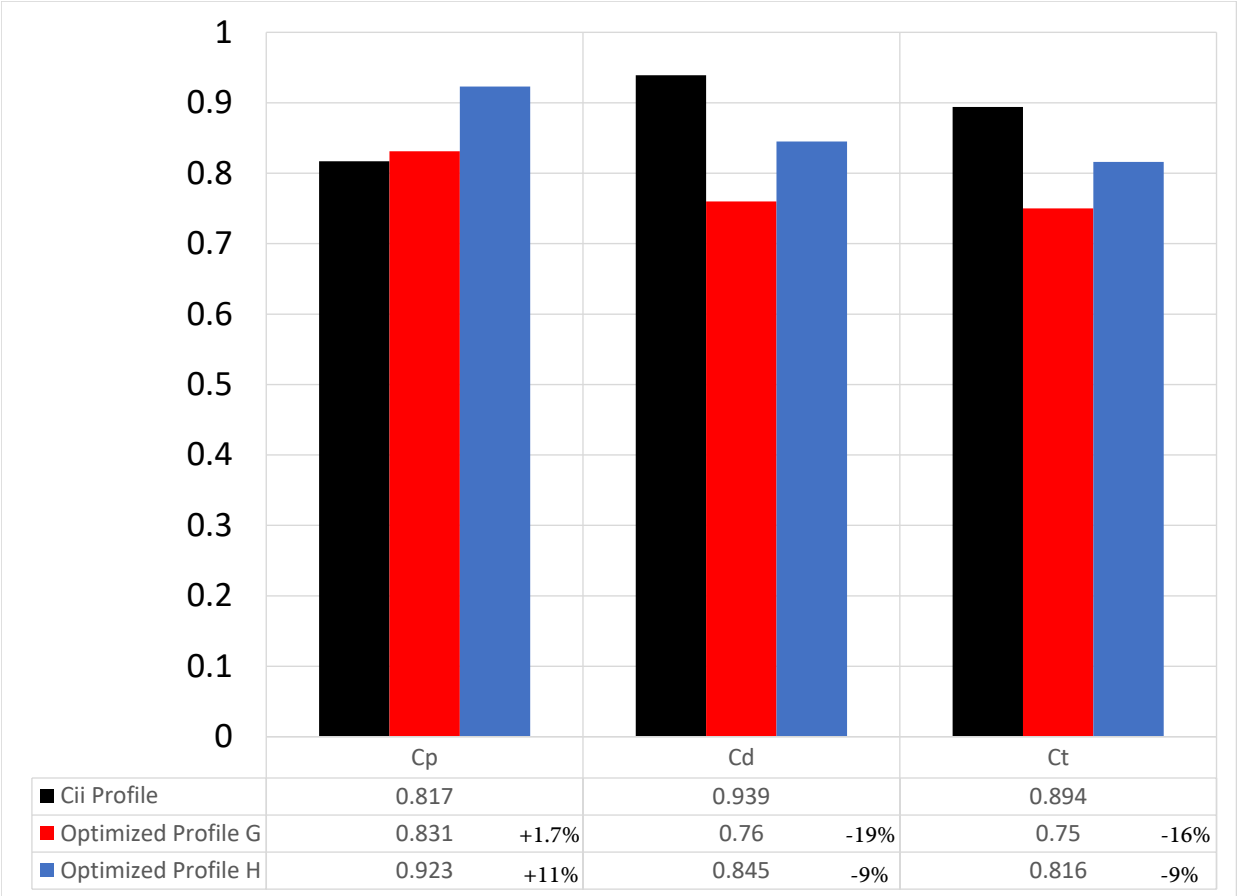

	Cp		Cd		Ct	
Cii Profile	0.817		0.939		0.894	
Optimized Profile G	0.831	+1.7%	0.76	-19%	0.75	-16%
Optimized Profile H	0.923	+11%	0.845	-9%	0.816	-9%

Figure 49 : Summary of table 20.

Case III - Shape Optimization Results IV

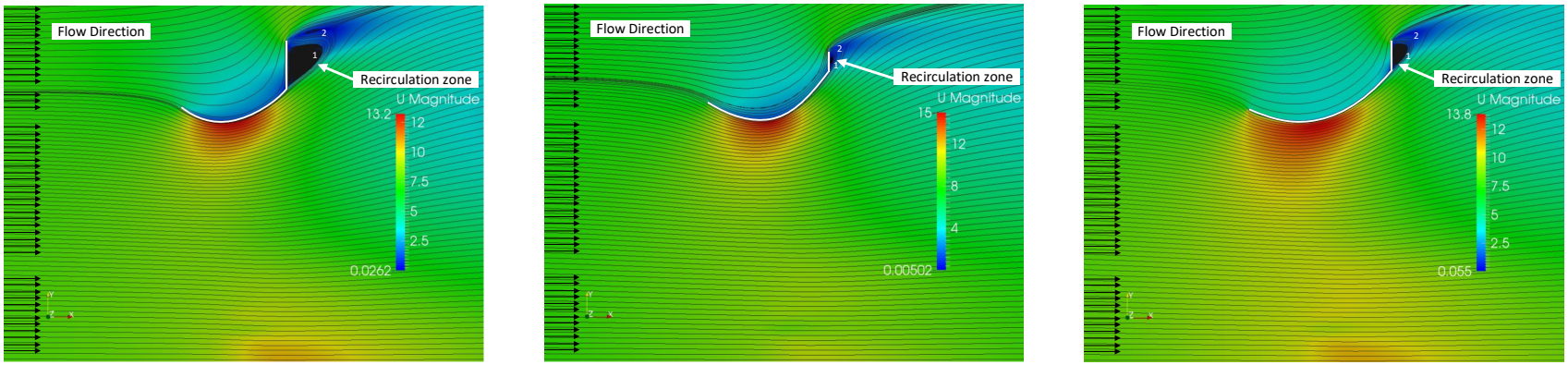

(a) Cii-type shroud. (b) Optimized profile G. (c) Optimized profile H.

Figure 50 : Velocity distribution with streamlines for *Cii* profile and optimized profiles G and H.

Case III - Shape Optimization Results V

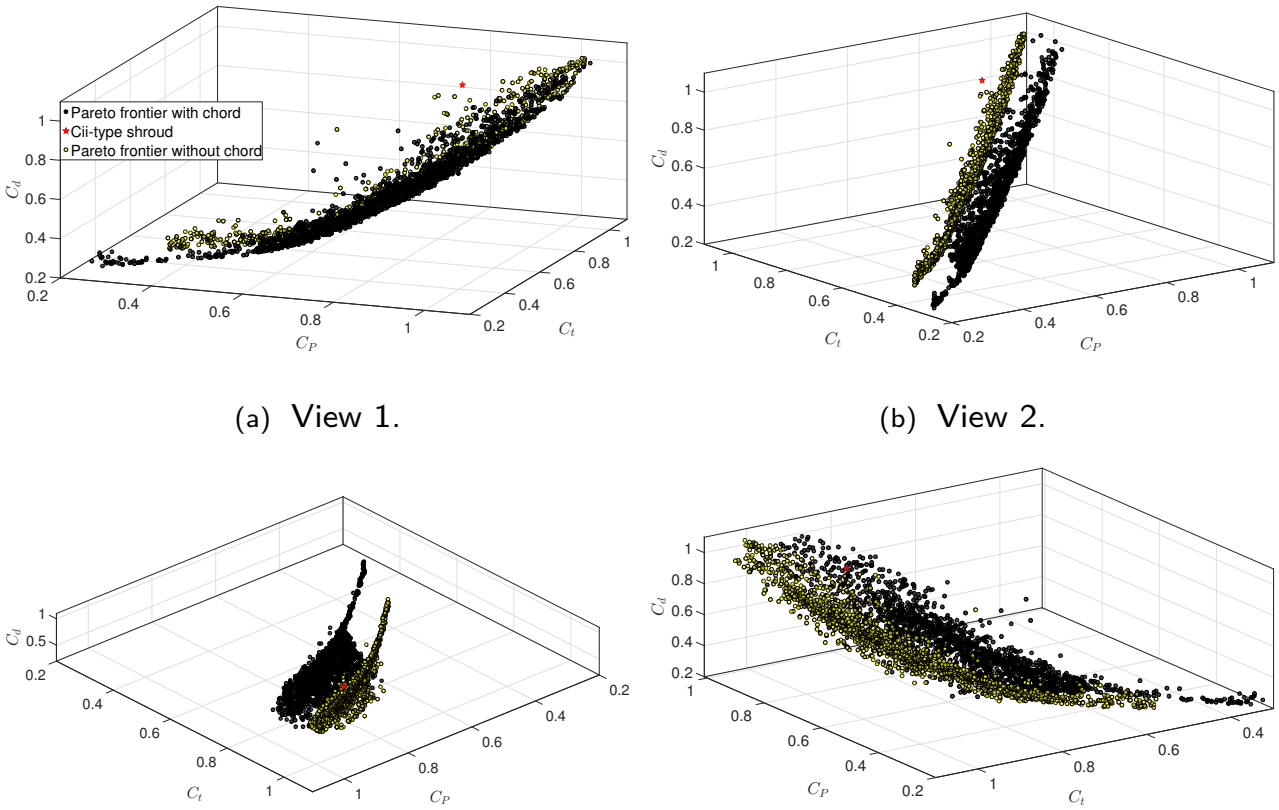

(a) View 1.

(b) View 2.

(c) View 3.

(d) View 4.

Figure 51 : Side views of the Pareto Frontiers obtained in Case II and Case III.

Conclusions

- A framework for the shape optimization of a wind-lens to reduce the drag and thrust forces and enhance the power production has been presented.
- To determine the pertinent coefficients of the shrouded turbine, the RANS equations augmented by a blade element moment (BEM) method have been employed.
- Further reduction in the computational cost of the simulations is achieved by taking advantage of the axisymmetry of the problem.
- The present method has been verified through grid convergence studies and validated by comparisons with wind tunnel test results as well as higher fidelity simulations.
- The shroud of the wind-lens is parameterized using piece-wise second-order polynomials and the twist and chord distribution are varied using Bezier curves.
- The developed axisymmetric RANS-BEM solver is coupled with DAKOTA's multi-objective genetic algorithm (MOGA) and results show that in fact more optimal shapes than the ones currently used can be found.

Future Work I

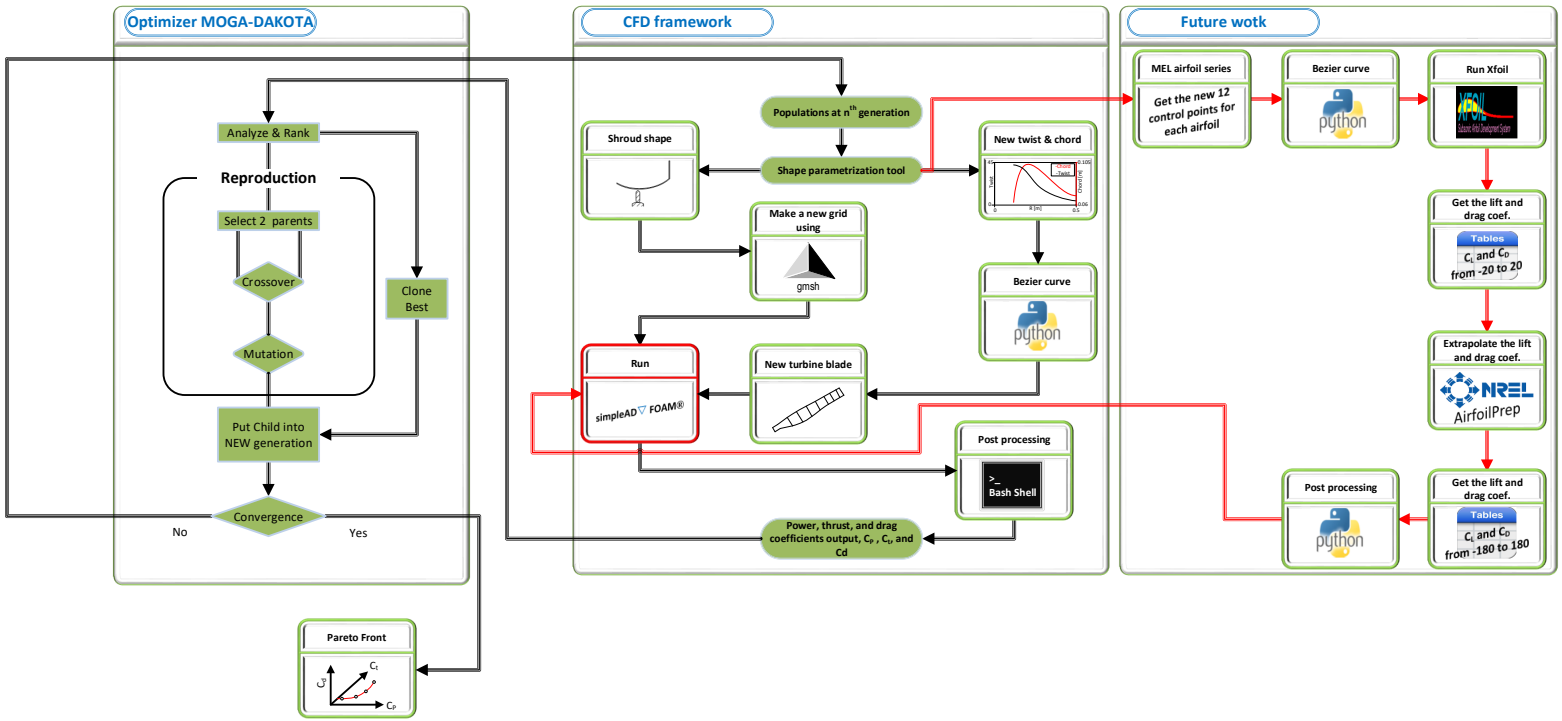

Figure 52 : Flow chart of an enhanced optimization framework.

Future Work II

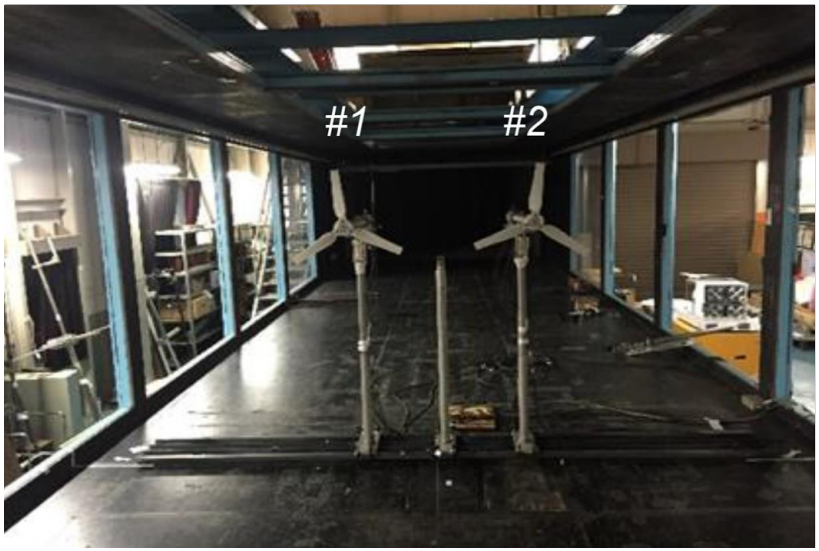

(a) Bare wind turbine setup.

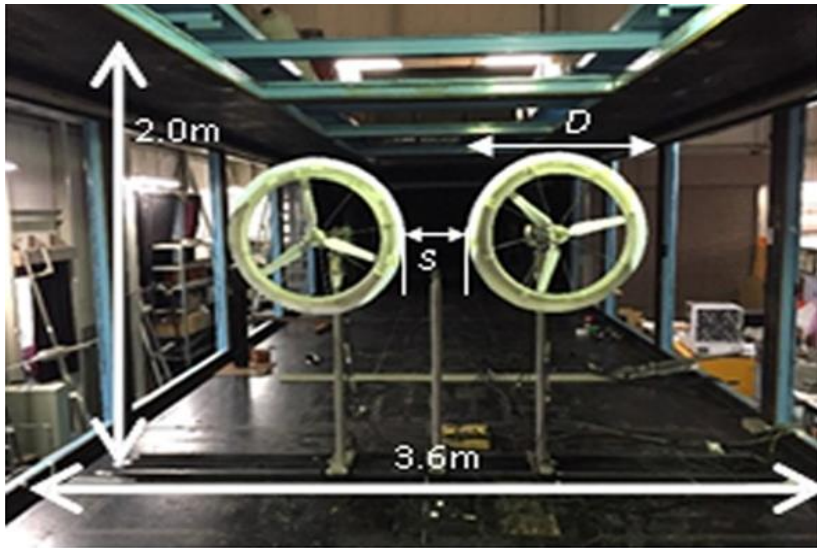

(b) Wind-lens turbine setup.

Figure 53 : Wind tunnel setup for ducted and unducted turbines in grid array [11].

Publications

Publications

- T. A. Khamlaj and M. Rumpfkeil, "Analysis and optimization of ducted wind turbines." Accepted by Journal of Energy.
- T. A. Khamlaj and M. Rumpfkeil, "Optimization study of shrouded horizontal axis wind turbine", in 2018 Wind Energy Symposium, 2018.
- T. A. Khamlaj and M. P. Rumpfkeil, "Theoretical analysis of shrouded horizontal axis wind turbines", Energies, Vol. 10, No. 38, p. 19, 2017.

Acknowledgement

To my adviser

- Dr. Markus Rumpfkeil

To the Dept. of Mech. and Aero. Eng. Including;

- Prof. Kelly Kissock
- Dr. Margaret Pinnell
- Prof. Jose Camberos
- Dr. Dave Myszka
- Lindsey Temple
- Sherri Alexander

To my Committee Members

- Prof. Kevin Hallinan
- Prof. Youssef Raffoul
- Dr. Andrew Chiasson

Questions?

References

[1] Y. Ohya, T. Karasudani, A. Sakurai, K.-i. Abe, and M. Inoue, "Development of a shrouded wind turbine with a flanged diffuser," *Journal of wind engineering and industrial aerodynamics*, vol. 96, no. 5, pp. 524–539, 2008.

[2] Y. Ohya and T. Karasudani, "A shrouded wind turbine generating high output power with wind-lens technology," *Energies*, vol. 3, no. 4, pp. 634–649, 2010.

[3] M. O. L. Hansen, N. N. Sørensen, and R. Flay, "Effect of placing a diffuser around a wind turbine," *Wind Energy*, vol. 3, no. 4, pp. 207–213, 2000.

[4] Y. Ohya, T. Uchida, T. Karasudani, M. Hasegawa, and H. Kume, "Numerical studies of flow around a wind turbine equipped with a flanged-diffuser shroud using an actuator-disk model," *Wind Engineering*, vol. 36, no. 4, pp. 455–472, 2012.

[5] L. Tossas and S. Leonardi, "Wind turbine modeling for computational fluid dynamics," *National Renewable Energy Laboratory (NREL), Technical Report No. NREL/SR-5000-55054*, 2013.

[6] J. F. Manwell, J. G. McGowan, and A. L. Rogers, *Wind energy explained: theory, design and application*. John Wiley & Sons, 2010.

[7] E. Kulunk, *Aerodynamics of wind turbines*. INTECH Open Access Publisher, 2011.

[8] H. MATSUMIYA, T. KOGAKI, N. TAKAHASHI, M. IIDA, and K. WASEDA, "Development and experimental verification of the new mel airfoil series for wind turbines," *Wind Energy Utilization Symposium*, vol. 22, pp. 92–95, 2000.

[9] M. Berger and Z. Wang, "International journal of computational fluid dynamics," *International Journal of Computational Fluid Dynamics*, vol. 19, no. 8, p. 547, 2005.

[10] B. Adams, M. Ebeida, M. Eldred, J. Jakeman, L. Swiler, A. Stephens, D. Vigil, and T. Wildey, "Sandia technical report sand2014-4633," 2014.

[11] Y. Ohya, J. Miyazaki, U. Göltenbott, and K. Watanabe, "Power augmentation of shrouded wind turbines in a multirotor system," *Journal of Energy Resources Technology*, vol. 139, no. 5, p. 051202, 2017.

Effect of Turbulence Models on Empty Diffuser

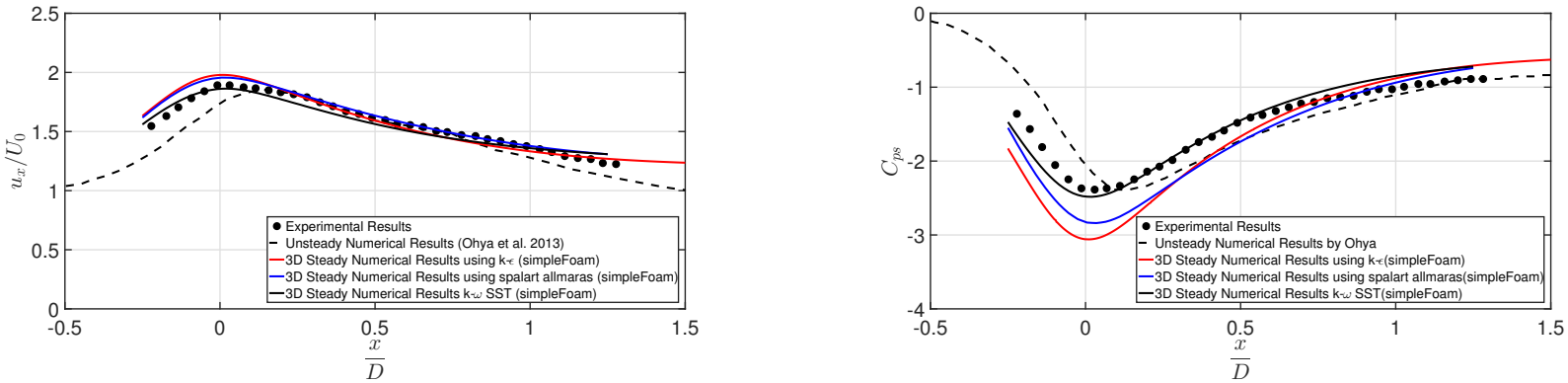

(a) Velocity distribution.

(b) Pressure distribution.

Figure 54 : Velocity and pressure distribution through an empty flanged diffuser using different turbulence models.

Conclusion

Even though the $k-\omega$ (SST) turbulence model results are in best agreement due to its ability to model boundary layer separation in adverse pressure gradients, it is not always practical to mesh down to $y^+ \simeq 1$ wall spacings when considering the overall computational cost required to search for an optimized shrouded design in the preliminary design stage. Therefore, the $k-\epsilon$ with standard wall functions is chosen.